THE IMPACTS OF ATMOSPHERIC RADIATION ON STUDIES OF PLANETARY HABITABILITY

A Dissertation
Presented to
The Academic Faculty

By

George D. McDonald

In Partial Fulfillment
of the Requirements for the Degree
Doctor of Philosophy in the
School of Earth and Atmospheric Sciences

Georgia Institute of Technology

August 2018

THE IMPACTS OF ATMOSPHERIC RADIATION ON STUDIES OF PLANETARY HABITABILITY

Approved by:

Dr. James Wray
School of Earth and Atmospheric Sciences
Georgia Institute of Technology

Dr. Sven Simon
School of Earth and Atmospheric Sciences
Georgia Institute of Technology

Dr. Irina Sokolik
School of Earth and Atmospheric Sciences
Georgia Institute of Technology

Dr. Paul Steffes
School of Electrical and Computer Engineering
Georgia Institute of Technology

Dr. Eric Lopez
NASA Goddard Space Flight Center

Approved: July 11, 2018

Hey now,

The past is told by those who win.

My darling,

What matters is what hasn't been.

Jimmy Eat World, "Futures"

ACKNOWLEDGEMENTS

It is a sincere honor and my greatest pleasure to acknowledge the following people:

Josh Méndez for being there for me, no matter what it was, and for helping me see the world in so many different ways.

Luju Ojha and Mary Beth Wilhelm for their camaraderie, insights, and so many fun times.

Sven Simon for his mentorship, guidance, always having an open door, and of course his love of Star Trek. Lucas Liuzzo, Slawa Kabanovic, Zach Meeks, Moritz Feyerabend and Hannes Arnold for their company. Tiegan Hobbs, Amy Williamson, Ryan Cahalan and anyone else who's friendly hi in the hallway helped me out on a rough day.

Alex Hayes for teaching me to be independent and quantitative. So much of the way that I do my work comes from you.

Paul Corlies for being a friend, and the best "collaborator" in the truest sense of the word. I look forward to finally having the time to focus more on the former.

Laura Kreidberg, Eric Lopez, and Tim McConnochie for teaching me so much. Joe Dufek for his support, and Carol Paty for letting me take one rein with the Planetary Seminar.

Claire Newman: from collaborator, to my public transit career sounding board to a friend.

Amelia Winner, Cansu Culha, Heather Chilton and Kim Halbert for being awesome lab/officemates (or labmate in spirit).

Dad and Mom for your support and understanding as I explore the so many things that I care about. Alice for always giving me new perspectives. Aunt Em and Aunt Judy for being willing to come along for the ride. 聰、おばあちゃんとおじいちゃん、いつもありがとう。

Ariel Brodsky and Justin Marut for being the best friends I could have asked for.

The entire Swim Atlanta Masters team at Georgia Tech, for keeping me sane at lunch, and for reinvigorating an important passion in my life. I will still be back at the pool every day to swim!

Andy Newman, Becky James and Kim Cobb for working to make Georgia Tech a safe place to bike.

Leslie Caceda, Shayna Pollock, Lori Sand and Cain Williamson at the Atlanta Regional Commission for letting me take a stab at work in public transportation and for all the fun conversations.

James Wray for his support. And for believing in a late convert to planetary science.

I would also like to acknowledge all of the free and open-source software without which this thesis could not have been completed. These include Python and its many user-made packages, Ubuntu, LaTeX, Inkscape, GIMP and QGIS.

The research in this thesis was conducted with government support under and awarded by the Department of Defense, Air Force Office of Scientific Research, National Defense Science and Engineering Graduate (NDSEG) Fellowship, 32 CFR 168a. In addition, I gratefully acknowledge support from the 2016 Kavli Summer Program in Astrophysics at UC Santa Cruz.

TABLE OF CONTENTS

LIST OF TABLES

LIST OF FIGURES

LIST OF SYMBOLS

$\eta_\oplus$	Frequency of Earth-sized rocky planets in habitable zones of Sun-like stars
λ	Wavelength
ρ	Density
σ	Standard deviation
τ_{sat}	Time at which the X-ray saturation phase ends
a	Planet semi-major axis
AD test	Anderson-Darling statistical test
AU	Astronomical unit
B_λ	Spectral radiance per unit wavelength
$B-V$	Blue filter minus visible filter color index
c	Speed of light
CDF	Cumulative distribution function
CDPP	Combined differential photometric precession (measurement of stellar noise)
CIA	Collision-induced absorption
CKS	California Kepler Survey
DISR	Descent Imager Spectral Radiometer instrument aboard the *Huygens* spacecraft
E	Energy
EUV	Extreme ultraviolet
$F_\oplus$	Solar constant
f_{cell}	Planet occurrence within a grid cell
$f_{cell,std}$	Standard deviation of f_{cell}
GCMS	Gass Chromatograph Mass Spectrometer aboard the *Huygens* spacecraft
h	Planck constant
H/He	Hydrogen/helium

I_λ	Intensity per unit wavelength
J_λ	Source function
K	Boltzmann constant
L_{bol}	Bolometric (broadband) luminosity
L_X	X-ray luminosity
L_J	J-band (1220 nm, near-infrared) luminosity
m	Mass
$M_\odot$	Solar mass
M_*	Stellar mass
MCMC	Markov-chain Monte Carlo method
$n_{pl,cell}$	Number of planets in a grid cell
$n_{*,eff,cell}$	Effective number of stars in a grid cell
PDF	Probability density function
r	Radius
$R_\oplus$	Earth radii
R_p	Planet radius
R_*	Stellar radius
T	Temperature
Z	Metallicity
x	Size parameter
VIMS	Visual and Infrared Mapping Spectrometer aboard the *Cassini* spacecraft
XUV	X-ray and extreme ultraviolet

SUMMARY

The conditions required for Earth-like life to emerge on a planet are thought to include the presence of liquid water, the availability of energy, the existence of organic material, and shielding from high energy charged particles. There are situations when determining whether these conditions exist on a planetary body is not possible without a detailed understanding of the radiative processes occurring in a planet's atmosphere. In this work, studies of the radiative flux and transfer within planetary atmospheres are carried out in order to elucidate whether certain planetary bodies may be habitable. The first section of this work quantifies the impinging X-ray flux on sub-Neptune sized planets in the *Kepler* spacecraft dataset. This study determines the conditions for such planets to be stripped of their primordial atmospheres, with implications for the stability of liquid water on their surfaces. In the second part, the absorption of light in the atmosphere of Saturn's largest moon Titan is modeled in order to understand how close to the surface one has to be to detect organic molecules of prebiotic relevance, including amino acids and nucleobases.

CHAPTER 1
INTRODUCTION

1.1 Planetary atmospheres: Controlled by the same physical processes

The majority of known planets, and some of their satellites, possess an atmosphere [de Pater and Lissauer, 2015]. This encompasses the planets in our solar system as well as extrasolar planets (exoplanets) of which measurements are sufficient to make such a determination.

The composition of planetary atmospheres varies significantly. At one end of the spectrum are the hydrogen/helium dominated atmospheres, similar to the sun and the protosolar nebular from which it formed in composition. These atmospheres are typically so dense that they form a fluid "envelope" which can dominate the planet's mass. On the other hand are the atmospheres of the terrestrial planets, these consist of primarily gases with molecular mass greater than three ($Z \geq 3$), with atmospheres that account for less than $<1\%$ of the mass of the planet. These are likely secondary atmospheres, i.e. they were not accreted directly from the protosolar nebula, but originated in the solid planetesimals that formed the planet and were later outgassed [de Pater and Lissauer, 2015, Baines et al., 2013].

Despite the differences in atmospheric composition and mass (and in turn, surface pressure), they are governed by the same physical and chemical processes. For example, the thermal stratification of the atmosphere and variations in the strength and location of solar insolation on the planet, leads to atmospheric circulation (i.e. winds). The focus of this thesis is on the ways in which solar radiation interacts with planetary atmospheres, and the implications this has for the habitability of planets or studies thereof. To examine this interplay, the physical processes controlling the interaction of stellar radiation with gases and particles, termed "radiative transfer," are of primary significance.

1.2 Radiative transfer

1.2.1 Stars as sources of electromagnetic radiation

Stars produce the overwhelming majority of radiation that the typical planet receives. Main-sequence stars, like the sun, generate notable fractions of their energy through the nuclear fusion of four hydrogen atoms to form one helium atom in the deep interior of the sun. The electromagnetic radiation that originates from this fusion is the result of the difference in mass between the product helium atom and the reactant hydrogen atoms and is governed by the equation:

$$E = mc^2 \tag{1.1}$$

The energy generated in a star's interior is transported by convection and through radiation to a region called the photosphere—the visible surface of stars where the majority of electromagnetic radiation reaching planets like the Earth originates. The effective temperature of the photosphere is approximately 5800 K [Liou, 2002]. In turn, stars produce electromagnetic spectra that can be approximated by a blackbody, an object wherein the absorption of radiation by molecules and its subsequent emission by the rotation and vibration of these same molecules is in equilibrium. A blackbody produces an emission spectrum whose wavelength dependence can be described by Planck's law:

$$B_\lambda(T) = \frac{2hc^2}{\lambda^5(e^{hc/K\lambda T} - 1)} \tag{1.2}$$

where λ denotes wavelength, T is the temperature of the blackbody, h is Planck's constant, and c is the speed of light.

In the case of the sun, blackbody radiation dominates its emission spectrum from the middle ultraviolet to radio wavelengths. This includes visible light, as well as most wavelengths used for remote sensing, including the infrared. Nevertheless all stars, including

the sun, produce an appreciable amount of X-ray radiation, extreme ultraviolet (EUV), and far ultraviolet (FUV). These are not generated through blackbody emission from the photosphere, but from the considerably hotter stellar corona. In the case of the sun, the corona is found $>$ 2000 km above the photosphere, extends for millions of kilometers, and possesses temperatures close to 10^6 K.

1.2.2 Absorption, emission and scattering

When light from a planet's host star interacts with a given particle in the planet's atmosphere, there are two possible scenarios. If the energy of the impinging photon, as described by:

$$E = \frac{hc}{\lambda} \tag{1.3}$$

is equivalent to either an electronic energy state of an atom or molecule, or a rotational or vibrational energy state of a molecule, the photon will be absorbed. If the atom or moleule absorbs more energy than is required to remove an electron, the atom/molecule will be ionized, with the additional energy in the form of kinetic energy imparted upon the free electron.

If the photon energy does not correspond to an energy state of the particle in question, the light will be scattered in different directions. The nature of this scattering, i.e. the angular pattern of light intensity resulting from the scattering event, depends on the size parameter which relates the size of the particle in question to the wavelength of the incident light:

$$x = \frac{2\pi r}{\lambda} \tag{1.4}$$

where r is the particle radius. If x $<<$ 1, the result will be Rayleigh scattering. Under this type of scattering, light will be scattered in all directions, but preferentially in the fore-

ward and backward directions in equal amounts. If x $\geq$ 1, the resulting scattering is termed Lorenz-Mie scattering. The angular pattern for Lorenz-Mie scattering is complicated, but involves preferential scattering in the forward direction.

1.2.3 The radiative transfer equation

Absorption and scattering are the fundamental processes that stellar light will undergo when passing through a planetary atmosphere, and an understanding of the two lead us to the general radiative transfer equation. Losses in signal due to both absorption and scattering are termed extinction. We consider radiation passing through a layer of thickness ds, with the intensity of the radiation entering the layer being I_λ. The loss in intensity of the radiation after exiting the layer is dI_λ due to absorption and scattering out of the beam, while J_λ is the source function and accounts for increases in intensity within the layer due to emission and multiple scattering events.

$$\frac{dI_\lambda}{k_\lambda \rho ds} = -I_\lambda + J_\lambda \tag{1.5}$$

k_λ is the mass extinction cross section (a quantification of the extinction properties of the atmosphere within the layer, in units of area per mass) for light with wavelength λ. ρ is the density of the atmospheric layer [Liou, 2002].

Use of the radiative transfer equation allows one to model and subsequently interpret spectra of a planetary atmosphere taken by remote sensing instruments, which are essentially signal returns (due to light collected by the instrument) as a function of wavelength. In albedo (often termed I/F) spectra, wavelengths with sharp reductions in albedo generally denote wavelengths where gas molecules in the atmosphere are absorbing light. In contrast, broad slopes of changing albedo over several micrometers (microns, μm) typically indicate losses (or gains) due to particle scattering. See Fig. 3.3 for sample albedo spectra.

1.3 Planetary habitability

Broadly, the conditions required for Earth-like life to emerge on a planetary body are thought to include the presence of liquid water, the availability of energy, the existence of organic material, and shielding from high energy charged particles [Raulin et al., 2009, See et al., 2014]. An exhaustive discussion of all the conditions that may make a planet habitable, including for potential life forms with wildly different chemistries from those on Earth, would be out of the scope of this thesis. Nevertheless, a couple key concepts/conditions that guide the search for habitable worlds based on the criteria listed above are discussed.

1.3.1 The habitable zone

On Earth, water is an essential solvent for all known life forms, as well as a means for transferring energy in metabolic processes. In particular, the exposure of water to the atmosphere has been considered an important criteria for the formation of complex prebiotic molecules that could eventually lead to the origin of life. This is both due to the availability of atmospheric gases as reactants as well as the presence of energy sources in the form of sunlight and lightning [Miller and Urey, 1959]. This is the region around a given star in which a planet can orbit while maintaining temperature conditions that allow for the presence of liquid water on its surface for millions of years [de Pater and Lissauer, 2015]. Placing additional scrutiny on planets located in the continuously habitable zone focuses much of the search for extraterrestrial life. Specifically, to planets that are thought to be the most likely to be inhabited based on our understanding of life on Earth.

1.3.2 The availability of organic molecules

Certain classes of organic molecules are known to be essential for terrestrial life. These include amino acids, sugar-like molecules, activated phosphates and nucleobases [Burton et al., 2012]. These molecules may be formed directly from molecules in a reducing atmo-

sphere as described by Miller and Urey 1959, or they may be delivered to a planetary body from asteroids which are known to be capable of hosting many of these molecules [Burton et al., 2012].

1.3.3 Shielding from high energy charged particles

High energy charged particles from stellar winds can be a significant impediment to life forms in two respects. Firstly, such particles can erode stable atmospheres, removing the pressure conditions required for surface liquid water. Secondly, they can cause frequent genetic mutations. For this reason, shielding from high energy charged particles, such as with a planetary magnetosphere, is a condition for a planet to be considered habitable [See et al., 2014].

1.4 Assessing the habitability of planets through an understanding of the radiative processes occurring in their atmospheres

There are situations when assessing one or more of the four conditions considered necessary for life to emerge on a planetary body is not possible without a detailed understanding of the radiative processes occurring in a planet's atmosphere.

Much previous work has stressed the importance of radiative processes in constraining habitability. As one example, Kasting et al. 1993 determined that the condensation of CO_2 in an atmosphere and the subsequent formation of clouds can considerably increase a planet's albedo, notably reducing the ability for such an atmosphere to be warmed. They use this process to define the inner edge of the habitable zone. Kasting et al. 1993 also indicated that high enough temperatures for a planet with an Earth-like composition will introduce large quantities of water into the stratosphere. This overcomes the diffusion restriction on the outward flow of hydrogen, allowing the hydrogen produced from photolyzed water vapor to escape to space, limiting the planet's ability to maintan surface water. Additional examples have arisen from considering the question of how long liquid

water has been stable on Mars's surface during its geologic history (and in turn how habitable it truly ever was). Attempts to address this question have involved extensive studies of the radiative properties of putative ancient Martian atmospheres which may have involved large concentrations of SO_2 [Johnson et al., 2008] or H_2 [Ramirez et al., 2013], and in turn how long such atmospheres would be able to sustain temperatures of 273 K or above (which would allow liquid water to be stable on the surface for a pressure of 1 bar).

Building upon the existing literature, **in this study I demonstrate that new constraints on the radiative processes occurring in an atmosphere can provide insights into the habitability of a planetary body, with a particular focus on cases where sufficient data to consider these questions has only recently become available**. This is accomplished by considering two examples pertaining to sub-Neptune sized exoplanets and Saturn's largest moon Titan:

1.4.1 Chapter 2: The sub-Neptune photoevaporation desert and its dependence on stellar type: Controlled by lifetime X-ray irradiation

Short-period sub-Neptunes with substantial volatile envelopes are among the most common type of known exoplanets. However, recent studies of the *Kepler* population have suggested a dearth of sub-Neptunes on highly irradiated orbits, where the planets are vulnerable to atmospheric photoevaporation. Physically, one expects this "photoevaporation desert" to depend on the total lifetime X-ray and extreme ultraviolet flux, which are the main drivers of atmospheric escape. In this chapter, I study the demographics of sub-Neptunes as a function of their lifetime exposure to high energy radiation and host star mass. I find that for a given present day insolation, planets around lower mass stars experience relatively more X-ray flux over their lifetimes ($\sim$100 $\times$ more for a planet orbiting a 0.3 $M_{\odot}$ star versus 1.2 $M_{\odot}$). Defining the photoevaporation desert as a region consistent with zero occurrence at 2 σ, I find that the onset of the desert occurs for integrated X-ray fluxes greater than 1.43 $\times 10^{22}$ to 8.23 $\times 10^{20}$ erg/cm^2 for planetary radii of 1.8 – 4 $R_{\oplus}$ (the desert boundary

depends on planet radius). I also compare the location of the photoevaporation desert for different stellar types. Critically, the onset of the desert occurs at lower bolometric flux values for lower mass stars, but at much more comparable locations in integrated X-ray flux space, suggesting that photoevporation driven by steady state stellar X-ray emissions is the dominant control on the location of the desert. **This may limit the ability of close-in rocky planets around M-dwarfs (for which the outer bound of the desert overlaps with the inner edge of the habitable zone) to sustain hydrogen/helium atmospheres, and in turn their ability to main surface liquid water.** Finally, I report tentative evidence for the sub-Neptune valley, first seen around Sun-like stars, for M & K dwarfs (main-sequence stars).

1.4.2 Chapter 3: Modeling transmission windows in Titan's lower troposphere: Implications for infrared spectrometers aboard future aerial and surface missions

Absorption from methane and other gases in Titan's atmosphere as well as particle scattering limits the visibility of the surface to only a handful of narrow windows in the near-infrared. This has limited the ability to identify specific compounds on the surface—to date Titan's bulk surface composition remains unknown. Further understanding of the surface composition would provide insight into geologic processes, photochemical production and evolution, and the biological potential of Titan's surface. However, the only way to obtain wider spectral coverage with which to study Titan's surface is by decreasing the integrated column of methane between the observer and the surface. To do this, future missions must operate at lower altitudes in Titan's atmosphere. Herein, we use a radiative transfer model to describe the expected improvement in the near and mid-IR reflectance measurements of Titan's surface for different possible mission architectures. We find that only for altitudes less than $\sim$1 km can significant widening of the windows ($\sim$10% wider compared to orbit) be obtained, while increases as large as $\sim$200% can be obtained at the surface. Improvements of this magnitude are only possible with the inclusion of onboard illumination.

Further, **we highlight what surface compounds not currently observable from orbit may be identified within widened tranmission windows near the surface. These range from simple nitriles such as cyanoacetylene, to building blocks for amino acids such as urea. The ability to identify these compounds on the surface would make it possible to assess whether all necessary building blocks for life exist on Titan's surface.**

1.4.3 Publications

The contents of this thesis have their foundations in 2 manuscripts prepared during my time at Georgia Tech:

1. **G.D. McDonald**, L. Kreidberg, and E. Lopez (Revised), The sub-Neptune desert and its dependence on stellar type: Controlled by lifetime X-ray irradiation, *The Astrophysical Journal*.

2. **G.D. McDonald***, P.M. Corlies*, A.G. Hayes, J.J. Wray, M. Ádámkovics, M.J. Malaska, M.L. Cable, J.D. Hofgartner, S. Hörst, L.R. Liuzzo, J.J. Buffo, R.D. Lorenz, E. Turtle (Submitted), Modeling transmission windows in Titan's lower troposphere: Implications for infrared spectrometers aboard future aerial and surface missions. *authors contributed equally.

In addition, although their contents are not included herein, the following manuscripts all touch upon the goal of this thesis and represent another sizable portion of my graduate research:

3. L. Ojha, M. Chojnacki, **G.D. McDonald**, A. Shumway, M.J. Wolff, M.D. Smith, A.S. McEwen, K. Ferrier, C. Huber, J.J. Wray, A. Toigo (2017). Seasonal slumps in Juventae Chasma, Mars, *Journal of Geophysical Research: Planets* 122.

4. J.S. Méndez Harper, **G.D. McDonald**, J. Dufek, M.J. Malaska, D.M. Burr, A.G. Hayes, J. McAdams, J.J. Wray (2017). Electrification of sand on Titan and its influence on sediment transport, *Nature Geoscience* 10, 260–265.

5. **G.D. McDonald**, A.G. Hayes, R.C. Ewing, J.M. Lora, C.E. Newman, T. Tokano, A. Lucas, A. Soto, G. Chen (2016). Variations in Titan's dune orientations as a result of orbital forcing, *Icarus* 270, 197–210.

CHAPTER 2

THE SUB-NEPTUNE DESERT AND ITS DEPENDENCE ON STELLAR TYPE: CONTROLLED BY LIFETIME X-RAY IRRADIATION

Published in modified form as:

G.D. McDonald, L. Kreidberg, and E. Lopez (Revised), The sub-Neptune desert and its dependence on stellar type: Controlled by lifetime X-ray irradiation, *The Astrophysical Journal*.

2.1 Introduction

The *Kepler* mission has confirmed the existence of over 2341 extrasolar planets [Thompson et al., 2017]. These discoveries provide valuable information about the distribution of planets in terms of their radii and semi-major axes. Of particular significance has been the discovery that given the current sample of close-in planets (5-50 day periods), the most common type are planets with radii in the range of 1 – 1.5 or 2 – 2.8 $R_\oplus$ (Earth radii) [Fressin et al., 2013, Petigura et al., 2013b,a, Fulton et al., 2017]. The former are typically referred to as super-Earths, we hereafter refer to the latter, as well as all planets in the range $1.8 < R_\oplus < 4$, as sub-Neptunes.

There is substantial evidence that these sub-Neptune planets represent a distinct population. Their boundary on the low radius end lies with evidence that planets with $R_\oplus > 1.5$ are not purely rocky in composition [Weiss and Marcy, 2014, Rogers, 2015], with those with $R_\oplus > 1.7$ in particular likely to require significant volatile envelopes to explain their low densities [e.g., Lopez and Fortney, 2014, Rogers, 2015, Fulton et al., 2017]. Subsequent studies have shown that these planets are best explained by models that have hydrogen/helium (hereafter H/He) envelopes atop Earth-like rocky cores [e.g., Wolfgang and Lopez, 2015, Chen and Rogers, 2016, Lopez, 2016, Owen and Wu, 2017, Jin and

Mordasini, 2017]. The upper bound of $< 4\ R_{\oplus}$ is motivated by the fact that these planets are typically significantly more massive [Weiss and Marcy, 2014, Wolfgang et al., 2016], which makes these planets considerably more resistant than smaller planets to atmospheric photoevaporation from high-energy radiation [Lopez and Fortney, 2013]. Despite their commonalities, studies of the mass-radius relations of these sub-Neptunes indicate that they are a diverse population, spanning a wide range of bulk densities and compositions [Weiss and Marcy, 2014, Wolfgang et al., 2016, e.g.,]. Understanding the set of conditions that will determine the envelope compositions and radii of these sub-Neptunes is a major area of research and will be key to our understanding of planet formation. Furthermore, it is important to recognize that the observed densities and radii are snapshots in time, and that an evolution across different portions of the parameter space is probable for many sub-Neptunes.

A specific process expected to have dramatic consequences on the evolution and properties of the sub-Neptune population is photoevaporation driven by high energy radiation, which has been suggested as a mechanism that would strip sub-Neptunes of their H/He envelopes over time [e.g., Baraffe et al., 2006, Jackson et al., 2010, Owen and Jackson, 2012, Lopez et al., 2012, Owen and Wu, 2013, Chen and Rogers, 2016]. This process is most impactful for sub-Neptunes on short-period orbits, where short means $\lesssim$ 10 days, in the case of Sun-like stars [Owen and Wu, 2013, Lopez and Fortney, 2013]. The mechanism of this photoevaporation process involves the photoionization of hydrogen from the absorption of X-rays and extreme ultraviolet radiation (XUV), which occurs at atmospheric pressures of around a nanobar, where a H/He-rich atmosphere becomes optically thin to the XUV [Yelle, 2004, Owen and Jackson, 2012, Murray-Clay et al., 2009]. The thermal excitation resulting from the photoionization can produce a hydrodynamic escape of the atmospheric hydrogen/helium. The impact of photoevaporation on the evolution of a short-period sub-Neptune can be substantial—low-mass planets with H/He dominated envelopes can have their envelopes completely stripped leaving only the solid core [Jackson et al., 2010, Owen

and Jackson, 2012, Lopez et al., 2012]. Non-thermal atmospheric stripping from stellar winds can be considered a competing process, but is found to be a secondary effect for planets with H/He-dominated atmospheres on close-in orbits [Airapetian et al., 2017].

However, the effects that photoevaporation-driven atmospheric escape can have on these planets vary significantly based on physical parameters such as planetary radius, planet mass, host star age and incident high-energy flux. For this reason, evolution models of sub-Neptunes, which account for the effects of hydrodynamic mass-loss and thermal contraction, have been developed to study this process. Studies that have run these models over large parameter spaces in incident bolometric flux and planetary mass have indicated a threshold above which planets will not be found after > 100 Myr due to photoevaporation-driven mass loss [e.g., Owen and Wu, 2013, Lopez and Fortney, 2013, Chen and Rogers, 2016]. The thresholds produced by these models are in good agreement with observations, which show a dearth of planets with low gravitational binding energies and large radii [Lopez, 2016, Owen and Wu, 2017, Jin and Mordasini, 2017].

Nevertheless, the sample of planets for which masses, and in turn binding energies, are known is relatively small. This has motivated searches for regions in planet radius space with a lack of sub-Neptune sized planets in the wider *Kepler* candidate dataset, where masses for most planets are unknown, but planetary radii and orbits have been measured. Sanchis-Ojeda et al. [2014] examined the population of *Kepler* planets with orbital periods less than one day, and noted a clear lack of planets larger than 2 $R_\oplus$, suggesting that photoevaporation could be responsible for this observation. More recently, Mazeh et al. [2016] defined the shape of the desert in the period-mass and period-radius planes, and Lundkvist et al. [2016] used a sample of planets around host stars with asteroseismic observations to suggest an absence of planets with bolometric fluxes greater than 650 times the solar constant (650 $F_\oplus$) and radii between 2.2 – 3.8 $R_\oplus$.

These studies have indicated the presence of a "photoevaporation desert" in the *Kepler* data, or a dearth of sub-Neptunes on close-in orbits. Nevertheless, there remains much to

be gleaned from observational constraints on the desert using the *Kepler* data. In particular, one expects the photoevaporation desert to depend on the X-ray and XUV flux received by a planet integrated over its lifetime, which is the main driver of atmospheric escape for these planets. Studies to date have defined the desert in the parameter spaces of orbital period and present-day bolometric flux. Here, we use the X-ray observations of Jackson et al. [2012] and Shkolnik and Barman [2014] to generate a lookup table of a star's lifetime-integrated X-ray luminosity as a function of its mass and age. Scaling the above by the semi-major axis of each planet of a detection-complete subset of the *Kepler* data, we define the photoevaporation desert in a lifetime-integrated X-ray flux parameter space. This allows us to quantify clear differences between the populations of rocky and gaseous planets, as well as to define the desert in a parameter space physically tied to the photoevaporation process, facillitating comparisons with the results of photoevaporation models. Furthermore, the effect of the stellar type of a planet's host star on its propensity for photoevaporation, and on the shape of the desert in the *Kepler* data has remained relatively unexplored. Owen and Wu 2013 briefly discussed these effects in a comparison of their photoevaporation model with the *Kepler* data. Our analysis significantly expands on this by defining desert bounds independent of a particular photoevaporation model using statistical criteria, in addition to utilizing significantly expanded and improved datasets.

The recent significant increase in the number of known exoplanets, specifically the 1284 new confirmed planets added to the general *Kepler* data by the uniform false positive probability analysis of Morton et al. [2016], along with the factor of three improvements in the precision of planetary radii, order of magnitude improvements in stellar fluxes, and first comprehensive dataset of planet ages provided by the California-Kepler Survey [Johnson et al., 2017] make this a well-timed occasion to improve observational constraints on the photoevaporation desert. With a sample size of 2341 detected planets, it is also possible to see how the desert varies as a function of the host star's spectral type.

We also investigate the photoevaporation valley, a gap in the *Kepler* planet data at 1.5

– 2 $R_\oplus$ first reported by Fulton et al. [2017], in the lifetime-integrated X-ray flux parameter space, as well as its dependence on stellar type. We find evidence suggestive of the sub-Neptune valley around M & K dwarfs, whereas previous detections have focused on Sun-like stars. The reader is referred to Fig. 10 of Fulton et al. 2017 for an illustrated comparison of the locations of the photoevaporation desert and valley, which are two distinct phenomena.

2.2 Methods

2.2.1 Lifetime-integrated X-ray flux as a function of stellar mass and age

Availability of extreme ultraviolet data

With the exception of the Sun, extreme ultraviolet (EUV, 10 – 124 nm) observations of stars are scarce. While studies have used models derived from solar observations to estimate XUV fluxes for old, Sun-like stars [Lecavelier Des Etangs, 2007, Sanz-Forcada et al., 2011], such extrapolations are not possible for other stellar types. Thus, we focus specifically on the evolution of the X-rays. X-rays are the primary driver for hydrodynamic escape [Owen and Jackson, 2012]. Furthermore, the XUV emission for Sun-type stars [Sanz-Forcada et al., 2011], and the trends of the near and far ultraviolet for M-dwarfs [Shkolnik and Barman, 2014], are all suggestive of the XUV evolution qualitatively following the same saturation and decay behavior as the X-rays.

Combining existing -X-ray data

To track the evolution of X-ray flux as a function of time for different stellar spectral types, we use the observationally derived relations in Jackson et al. [2012] and Shkolnik and Barman [2014]. Jackson et al. [2012] used X-ray survey observations of open clusters to report the ratio of the X-ray to bolometric luminosity across stellar ages of 10 Myr to 4.5 Gyr, with bins spanning stellar spectral types from K5 to F0. Shkolnik and Barman 2014

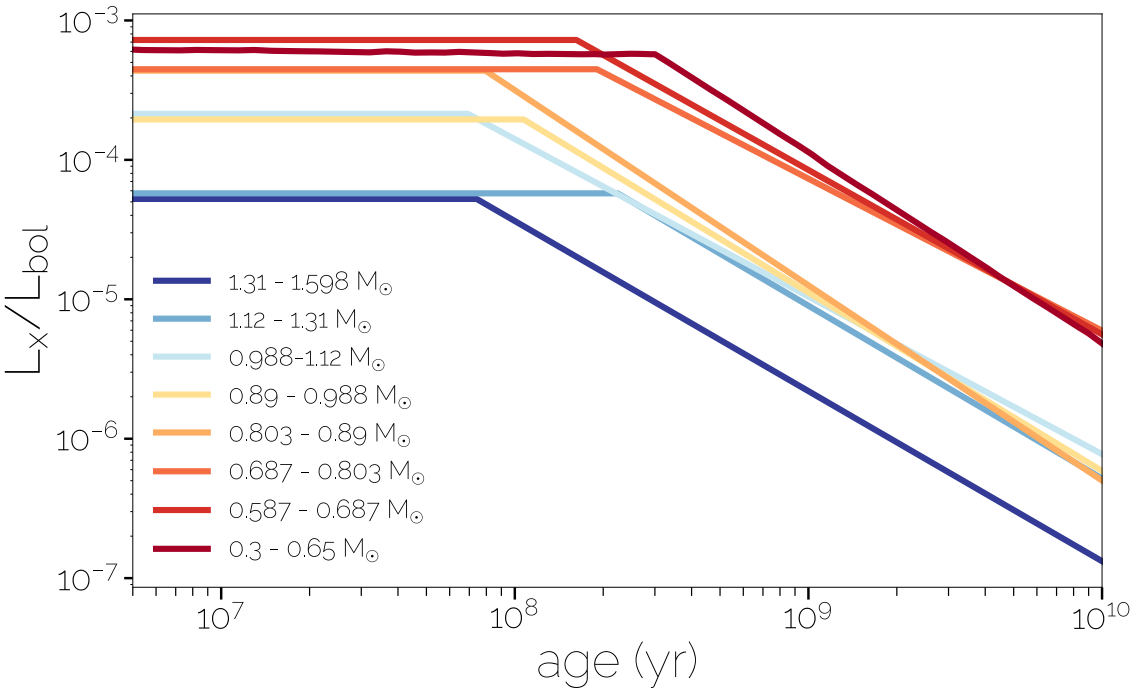

Figure 2.1: X-ray evolution as a fraction of total luminosity for different stellar types. Data are from Jackson et al. [2012] and Shkolnik and Barman [2014].

used *ROSAT* (Röntgensatellit) observations to determine the X-ray to J-band (centered at 1.25 μm) flux ratio for M4 to K4 spectral types with stellar ages of 10 Myr to 5 Gyr. Combining these two data sets, the rough range of stellar masses for which the lifetime X-ray evolution has been measured is 0.3 – 1.4 $M_\odot$. These data measure the steady state X-ray emission and do not account for additional X-ray emissions from large flares or coronal mass ejections.

The same trend of a saturated phase of X-ray emission early in the lifetime of the star, tens to hundreds of millions years, followed by a decay is found across all stellar spectral types (Fig. 2.1). The main difference between spectral types is twofold: as stellar mass decreases, stars saturate with a greater proportion of their luminosity in the X-rays, while the saturation phase also increases in duration [Jackson et al., 2012, Shkolnik and Barman, 2014]. Both trends are visible in Fig. 2.1. Although this behavior is not monotonic across spectral types as a result of the uncertainties in the observations, the overall trend is apparent. We note that the binning by spectral type of Jackson et al. [2012] was carried

using $B-V$ color—we convert the main sequence $B-V$ color bins to stellar mass bins solely for reference in Fig. 2.1. The conversion from $B-V$ color to stellar mass varies as a function of stellar age, and the full treatment for our calculation of lifetime-integrated X-ray fluxes is more complex and described in detail in section 2.2.1.

Both Jackson et al. [2012] and Shkolnik and Barman [2014] parametrize the X-ray to bolometric luminosity ratio (L_X/L_{bol}) and X-ray to J-band luminosity (L_X/L_J) respectively, as a function of stellar age (for a given spectral type) by fitting a broken power law. The saturated phase is fit by a flat line, and the subsequent decay is fit with a power law. The uncertainties in the X-ray measurements of open clusters and field stars, which are used to define individual data points, can span orders of magnitude for the least precise measurements, with the precision varying as a function of stellar age and spectral type, both parameters that are independent variables in our analysis. In order to accurately account for these errors in our calculations, we carry out a Markov-chain Monte Carlo (hereafter MCMC) fit to all data points in each of the stellar bins defined by Jackson et al. [2012] and Shkolnik and Barman [2014]. In carrying out the MCMC, we take the least squares fit of a broken power law (using a piecewise function to fit to all data points simultaneously) to the data and their errors in L_X/L_{bol} to be the maximum likelihood result.

The fit itself is carried out in the log (age[yr]) and log(L_X/L_{bol}) parameter space, such that we are fitting to the data with a piecewise function of two lines (as in Fig. 2.1), one with a slope of zero representing the saturation phase, and a line of negative slope representing the decay in X-ray luminosity as a function of time. The parameters that we fit for are the log(L_X/L_{bol}) intercept for the line of negative slope, the logarithm of the time at which the saturation phase ends (log τ_{sat}), and the slope of the line representing the X-ray luminosity decay—under the condition that the piecewise function is continuous. These fits, which are carried out in logarithmic space, are then converted to the following: the ratio of X-ray to bolometric, or J-band for Shkolnik and Barman [2014], luminosity during the saturation phase (L_X/L_{bol}), the time at which the saturation phase ends τ_{sat} and the power-law index

α for the decay in L_X/L_{bol} after τ_{sat}. This approach returned fit parameters in many cases identical to those reported in Jackson et al. [2012] and Shkolnik and Barman [2014]. So as to ensure agreement of our maximum likelihood fits with those reported in Jackson et al. 2012, we carried out the "lower weighting" of data points referenced with arrows described in Fig. 2 of Jackson et al. [2012]—we found that multiplying the errors for these data points by a factor of five produced fit parameters in closest agreement with theirs.

With our maximum likelihood fit parameters in hand, we sampled the parameter space with a Markov-chain Monte Carlo of 100 samplers over 1200 steps using the `emcee` routine of Foreman-Mackey et al. 2012. Discarding the first 200 steps during which the samplers have not yet sampled the full parameter space, we are left with 100,000 fits, comprising three posterior probability distributions, one for each fit parameter. We randomly sample the fit parameters for 1000 of the fits, taking note that this number of subsamples still accurately represents the shape of the original posterior probability distributions. These 1000 fits are used to account for the effects that the errors in the X-ray measurements have on our calculation of lifetime-integrated X-ray luminosities and fluxes.

Stellar evolution and calculation of a lifetime-integrated X-ray luminosity lookup table

We ultimately seek to calculate estimates of the lifetime-integrated X-ray flux for all planets in the *Kepler* sample. However, the calculation of lifetime-integrated X-ray flux for each planet, as well as a Monte Carlo sampling of each planet's errors, is precluded by the time-intensive nature of the calculation. Because the resolution of the stellar masses in the isochrones that we use as inputs, as well as the ages at which lifetime-integrated X-ray fluxes have been measured, are known, we are aware of the maximum resolution at which lifetime-integrated X-ray luminosities can be accurately calculated as a function of stellar mass and age. For this reason, we precalculate a lookup table—an array of lifetime-integrated X-ray luminosities for given stellar masses and ages, which can be quickly queried for use in estimating the lifetime-integrated X-ray flux for each *Kepler*

planet.

As discussed in section 2.2.1, the data on X-ray evolution are reported in terms of L_X/L_{bol} or L_X/L_J. As such, it becomes necessary to model the temporal evolution of the bolometric and J-band luminosities for the stellar types of interest, in order to determine the temporal evolution of the X-ray luminosity itself. Stellar isochrone models are well suited for this, and we use the *PARSEC* isochrones obtained from the `CMD 2.8` web interface [Bressan et al., 2012, Chen et al., 2014]. We utilize the *PARSEC* isochrones for their fine mass resolution (~ 0.03) over our $0.3 < M_{\odot} < 1.4$ range of interest, as well as the availability of tracks for stars with non-solar metallicities.

In generating our lookup table, we define 40 linearly spaced mass bins over the solar mass range $0.3 < M_{\odot} < 1.4$, as well as 50 different stellar ages which we integrate up to. 20 ages are logarithmically spaced between 200 Myr (limited on the low end by the lowest ages in the *PARSEC* isochrones) and 1 Gyr, and the final 30 are linearly spaced fom 1 – 10 Gyr so as to finely sample the age range which most *Kepler* planets fall in (Johnson et al. [2017], also see Fig. 2.3). Finally, 5 bins in metallicity are specified at $Z = 0.0025$, 0.0075, 0.0125, 0.0175 and 0.03.

For each mass, age and metallicity bin, we track the star's luminosity and $B - V$ color at each time-step in the isochrone (spaced as log(time[yr]) = 0.03). At each time-step, we use the $B - V$ color to place the star in the appropriate bin of X-ray evolution as described in section 2.2.1. We then multiply the isochrone luminosity by one of the L_X/L_{bol} ratios among the 1000 fits generated for this bin in section 2.2.1. This leaves us with L_X as a function of time, which we integrate over the lifetime of the star by quadrature (a numerical integration using polynomial interpolation functions) to get a lifetime-integrated X-ray luminosity. For stars of $M_* > 0.9M_{\odot}$ that are older than 1 Gyr, we monitor the evolution of the star's stellar effective temperature to determine whether it leaves the main sequence during its lifetime. We consider a greater than 10% change in stellar effective temperature vs. log(time[yr]) to be a signature that the star has left the main sequence. This criteria

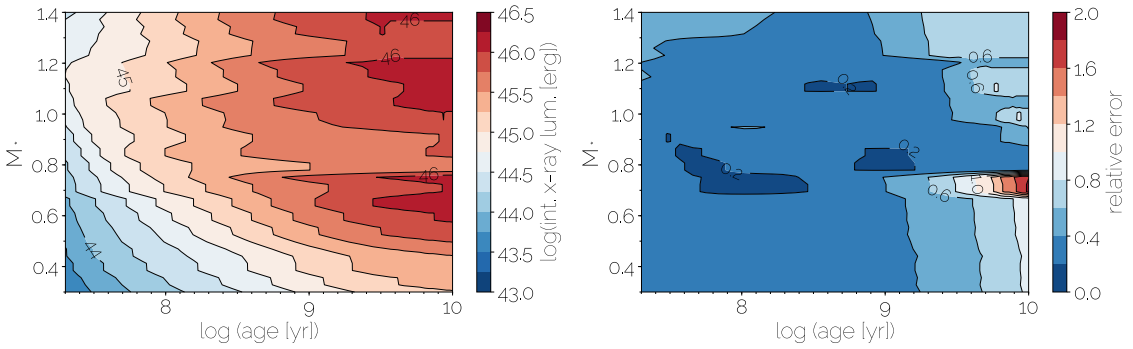

a) b)

Figure 2.2: a) Lookup table of integrated X-ray luminosity as a function of stellar mass and age, using fits to the observational relations of Jackson et al. [2012] and Shkolnik and Barman [2014]. This table is for a stellar metallicity of $Z = 0.0175$, and shows the mean luminosities of 1000 realizations of fits to the data. b) Relative errors on the X-ray luminosity calculated from the 1000 realizations.

accurately captures the point in time before dramatic changes to the star's other physical parameters, e.g. R_*, also occur. We stop the integration of lifetime-integrated X-ray flux at the time that the star has left the main sequence, due to the lack of comprehensive observations of X-ray emissions from post main-sequence stars. This process of calculating lifetime-integrated X-ray luminosity is repeated for all mass, age and metallicity bins, and then repeated for each one of the 1000 sets of X-ray evolution fit parameters from section 2.2.1. This effectively provides 1000 realizations of the lookup table that sample the extent of the errors in the X-ray measurements.

In Fig. 2.2, we show our lookup table for our closest-to-solar metallicity bin ($Z = 0.0175$). Fig. 2.2a shows the mean lifetime integrated-X-ray luminosity of the 1000 realizations in X-ray evolution fit parameters, while Fig. 2.2b shows the relative error in the lifetime-integrated X-ray luminosities. The physical implications of the results in the lookup table will be discussed in section 2.3.1. Over the majority of the parameter space, relative errors are around 30%, although for stars of $M_* \sim 0.7 M_\odot$ older than 3 Gyr, relative errors are greater than 100%. This is due to poor constraints on the post-saturation phase X-ray evolution for this particular bin of $0.935 < B - V < 1.275$ (see Jackson et al.

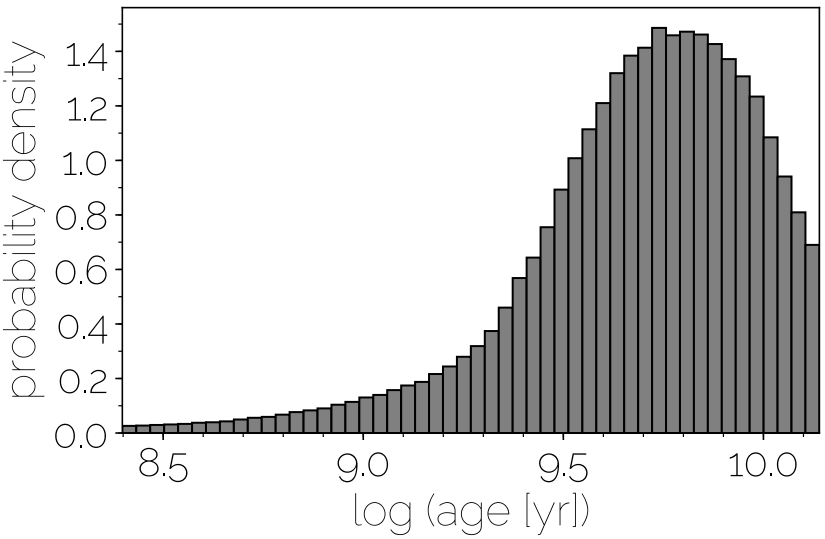

Figure 2.3: A histogram of the relative frequencies of all host star ages from the California Kepler Survey (CKS, Petigura et al. 2017, Johnson et al. 2017). In order to account for the errors in the determination of ages, 1000 realizations of the age of each planet are included in the histogram.

[2012] Fig. 2f).

Although we utilize and report results using the *PARSEC* isochrones due to their mass and metallicity resolution, as well as their direct outputting of $B-V$ color, we have verified our results by repeating the above analysis using the Baraffe et al. [2015] stellar isochrones, combined with estimates of $B-V$ color from model stellar effective temperature using the observations of Pecaut and Mamajek [2013]. We find that our results are largely independent of the isochrones used.

2.2.2 Lifetime-integrated X-ray fluxes for *Kepler* candidates

Kepler data

In this section, we calculate the lifetime-integrated X-ray flux for stars in the *Kepler* sample. We utilize two sets of *Kepler* data. For the purposes of defining the photoevaporation desert with the greatest possible precision, we use data from the California Kepler Survey [Petigura et al., 2017, Johnson et al., 2017]. The California Kepler Survey (abbreviated

CKS) used follow-up spectroscopic observations to improve the precision on the stellar parameters of 1305 *Kepler* stars, and in turn the measurements of 2025 *Kepler* planets. The CKS measurements have resulted in a factor of $\sim$3 improvement in the precision on measurement of stellar masses, as well as a factor of $\sim$2 improvement in stellar radius precision that has resulted in a factor of $\sim$2 improvement in precision for the planetary radii (using the planet-to-star radius ratios from the latest Q1-17 DR 25 *Kepler* catalog, Johnson et al. [2017]). Furthermore, the CKS is the first comprehensive survey of *Kepler* stellar ages (see Fig. 2.3), increasing the sample size of stars with ages by almost two orders of magnitude over previous studies. This enables, for the first time, calculating estimates of parameters such as lifetime-integrated X-ray flux for a majority of planets in the *Kepler* dataset.

Because the CKS is a magnitude limited survey (less than magnitude 14.2 in the *Kepler* bandpass, Petigura et al. [2017]), it excludes most low-mass stars from the *Kepler* sample, and consists largely of Sun-like stars. To explore differences in the photoevaporation desert and valley as a function of stellar type, we use the latest release of the general *Kepler* dataset. The recent calculation of uniform false positive probabilities (FPP) for all *Kepler* Objects of Interest by Morton et al. 2016 has resulted in a large increase in the number of confirmed *Kepler* planets, totaling 2284 planets. We utilize the sample of planets confirmed by the analysis of Morton et al. 2016, along with the stellar and planet properties from the *Kepler* Q1-17 DR 25 catalog when examining differences in properties among stellar types.

Propagating the Kepler planet uncertainties through our calculation of lifetime X-ray fluxes

The relative errors on the properties of the *Kepler* planets and host stars can be large. Even with the improved precision of the California Kepler Survey, the typical 5% errors on stellar masses, 11% uncertainty factor on stellar radius, and factor of two uncertainty in ages can result in significant variations in estimates of lifetime-integrated X-ray flux for a given planet. The effect of these errors on defining a region free of planets (the photoevaporation

desert) must be taken into account, especially when dealing with samples limited to several dozen to a couple hundred planets (the reason for the smaller samples of planets will be discussed in section 2.2.2). The consideration of errors becomes even more important when using the regular *Kepler* sample to compare properties dependent on host star stellar type, in which typical errors on planet radii are $\sim 40\%$ [Johnson et al., 2017].

In consideration of these errors, as well as the fact that our calculations of lifetime-integrated X-ray luminosities rely on numerical integration of binned observational data (making it impractical to propagate errors), we take a Monte Carlo approach to modeling the errors on planets. We replace each planet in the specific dataset being considered (CKS or Q1-17 DR 25 and Morton et al. [2016]) with 1000 "fractional planets", each weighted to be 1/1000th of a planet. The physical parameters for each of the 1000 planet fractions and their respective host star are determined by taking posteriors directly from the relevant table: the Q1-17 DR 25 stellar catalog [Mathur et al., 2016], the Q1-17 DR 25 planet catalog [Hoffman and Rowe, 2017], or the California Kepler Survey (Petigura et al. [2017], Johnson et al. [2017], posteriors were provided by Erik Petigura upon request). The lifetime-integrated X-ray flux for each fractional planet is determined by using the lookup table described in section 2.2.1 to get a lifetime-integrated X-ray luminosity for its Monte Carlo'd host star. 1000 realizations of the lifetime X-ray luminosity lookup table were previously generated to account for uncertainties in the X-ray observations. Each of the 1000 realizations of the lookup table are used for each of the 1000 planet fractions representing one planet, such that the uncertainties in the lifetime X-ray luminosity are propagated. The time-integrated X-ray luminosity for a fractional planet is then divided by the posterior for its semi-major axis to get a time-integrated X-ray flux.

For the CKS data, posteriors of the ages of each planet's host star are available, and drawn from for each fractional planet. In the case of the Q1-17 DR 25 catalog, ages have not been measured. While many of the G type host stars in the catalog have ages that have been measured by the CKS, the majority of the M & K type stars, which we wish to compare

to, have no age information. In order to treat the ages, and in turn the lifetime integration over X-ray luminosity, consistently for all stellar types in the Q1-17 DR 25 catalog, we take the approach of randomly drawing an age for the host star of each fractional planet in the catalog from the full distribution of ages of the CKS sample (whereby the errors in the CKS ages are accounted for by including 1000 age posteriors for each star in the CKS sample). Because the ages measured by the CKS form a single unimodal distribution around ~ 6 Gyr (Fig. 2.3), a random drawing of ages for each host star in the Q1-17 DR 25 catalog should produce similar average behavior over a large sample.

Selecting a subsample complete near the desert edge

Using the lifetime-integrated X-ray fluxes calculated for each of the 1000 fractional planets, we calculate planet occurrences in the parameter space of planet radius (R_p) vs lifetime-integrated X-ray flux.

Planet occurrence calculations must account for the completeness of the *Kepler* dataset [Howard et al., 2012], i.e. whether every planet is likely to have been detected around the sample of stars of interest. We elect to focus our analysis on a subsample of the *Kepler* dataset that is complete at the edge of the photoevaporation desert, such that the shape of the desert that we define should be unaffected by pipeline completeness. We follow the methodology of Wolfgang and Lopez [2015], who performed SNR calculations for transits to define a set of host stars for which the detection of sub-Neptunes is complete. Because our interest is in photoevaporation, which occurs for planets on short periods, we elect to further restrict our period sample, allowing us to relax the restrictions of Wolfgang and Lopez 2015 on stellar noise (combined differential photometric precision, or CDPP). With this adjustment, the cuts we make to select a desert-complete sample are stellar radius $R_* < 1.2R_\odot$, $R_p > 1.2R_\oplus$, period $<$ 10 days and CDPP binned to the timescale of the planet's transit $<$ 200 ppm (compared to the period $<$ 25 days and CDPP $<$ 100 ppm cuts of Wolfgang and Lopez 2015). The cuts are carried out on the fractional planets themselves.

Table 2.1: The number of planets as well as the average number of stars each planet could be detected around (this varies by planet, based on its host star's noise) for each of our samples of interest. These samples are the California Kepler Survey and the Q1-17 DR 25 and Morton et al. 2016 sample including its stellar subsamples. *The number of planets can deviate from an integer because we consider individual fractional planets to sample measurement uncertainities, these are weighted such that 1000 fractional plaenets are the equivalent of one planet.

Data set	Planet sample size	Average stellar sample size
California Kepler Survey	155.0	8.1×10^4
Q1-17 DR 25 and Morton et al. 2016	156.4	7.8×10^4
M & K subsample	52.9	1.2×10^4
G subsample	97.4	5.2×10^4
F subsample	6.2	1.4×10^4

The number of planets, as well as stars, left by the above cuts are tabulated in Table 2.1 for the two datasets we use, as well as their stellar subsamples. Around 150 planets form the sample with host stars of all spectral types for both the CKS and the Q1-17 DR 25 and Morton et al. 2016 datasets. The extremely small sample size of planets around F type stars (6.2) is a result of a large fraction of these stars having left the main sequence for the *Kepler* ages, and in turn being discarded. We include our analyses on the F type stars for reference, but focus our interpretations on the M & K and G type subsamples due to their larger sample sizes.

2.2.3 Constraining the shape of the photoevaporation desert

Calculating occurrence

We create two grids to calculate planet occurrence: one in the parameter space of planet radius and lifetime-integrated X-ray flux, and the other in planet radius and bolometric flux space, for comparison with previous studies. We define our grids so that the parameter space defined by our bounds in bolometric flux are equivalent to the bounds defined for

lifetime-integrated X-ray flux, for a solar mass star of age 5 Gyr (defined at the low end to correspond to our 10 day period cut, at the high end based on the maximum lifetime-integrated X-ray flux calculated for the *Kepler* planets). To calculate the occurrence within a given grid cell, we adopt the methodology of Howard et al. 2012. We reproduce equation (2) from Howard et al. [2012], where the average planet occurrence within a cell of R_p and lifetime-integrated X-ray flux is:

$$f_{cell} = \sum_{j=1} n_{pl,cell} \frac{1/p_j}{n_{*,j}} \tag{2.1}$$

where $p_j = (R_*/a)_j$ is the transit probability for fractional planet j, with a being its semi-major axis. Because we sum over fractional planets, we weight each fractional planet to be 1/1000th of a full planet. $n_{*,j}$ is the number of stars that pass the cuts described in section 2.2.2 for the transit duration of the specific fractional planet under consideration.

Again, following Howard et al. [2012], we calculate the error in f_{cell} using binomial statistics. The standard deviation of f_{cell} is calculated from the probability distribution of drawing $n_{pl,cell}$ planets from $n_{*,eff,cell} = n_{pl,cell}/f_{cell}$ effective stars:

$$f_{cell,std} = \sqrt{n_{*,eff,cell} f_{cell,std}(1 - f_{cell,std})} \tag{2.2}$$

In reporting occurrences, we choose to report occurrence densities [Foreman-Mackey et al., 2014], where we are dividing the occurrence in each grid cell by the area of the grid in dR_p dFlux. This way, the values that we report are not dependent on the specific grid resolution that is chosen.

Characterizing the occurrence desert in two dimensions

We wish to search for a region of the parameter space with no planets, an occurrence desert. We expect a desert to exist for gaseous planets at high fluxes due to atmospheric escape [e.g., Owen and Wu, 2013, Lopez and Fortney, 2013, Chen and Rogers, 2016].

Given the large uncertainties on planet properties and fluxes, no region of the occurrence grid is exactly zero. To define the desert, we take the largest region of the occurrence grid that is consistent with zero at two sigma confidence. To find this region, we adopt the following algorithm. We start by taking note of the planet occurrence and its 2σ deviation in the cell of largest planetary radii (3.9 – 5 $R_\oplus$) and highest flux value (i.e. the upper right corner of the plots in Fig. 2.7). Due to the low occurrence and large uncertainties arising from the small number of planets in this cell (typically a handful of fractional planets), its occurrence is always consistent at the 2σ level with an occurrence of zero. This cell is considered the starting point for our desert. We then consider the occurrences in each of the grid cells sharing one border with our initial desert grid cell. The cell with the lowest occurrence is added to the desert. The total occurrence in the new desert consisting of two cells is calculated, and the standard deviation of the desert occurrence is recalculated using binomial statistics for all fractional planets in the desert grid cells, using equation 2.2. This process is repeated until we have drawn the largest possible region that is still consistent with an occurrence of zero at the 2σ level. We define this region to be the desert.

We initially calculate an occurence grid with a resolution chosen such that the largest relative errors in occurrence per grid cell for the full CKS and Q1-17 DR 25 and Morton et al. 2016 datasets are one order of magnitude; we use this grid in studies of the photoevaporation desert. In investigating the photoevaporation valley, we select a much finer resolution that lends itself to much larger relative errors in individual grid cells. However, as our interest for the valley is in occurrence summed over the radius axis, the magnitude of the relative errors for the summed occurrences still meet our criteria of < 1 dex.

Characterizing the occurrence desert in one dimension

We facilitate comparison of the photoevaporation desert among different parameters, present-day bolometric flux vs lifetime-integrated X-ray flux, as well as among different subsamples of stellar type and planet radius, by examining our full data set of planets in one dimen-

sion. We take all fractional planets from our data set of interest with R_p: $1.8 < R_\oplus < 4$ (our definition of sub-Neptunes), and generate a cumulative distribution function (CDF) over the flux dimension, beginning at the fractional planets with highest fluxes where our sub-sample is immune to pipeline incompleteness.

We wish to compare the CDFs for bolometric flux vs lifetime-integrated X-ray flux, which are parameters with different units. For this comparison, the bolometric flux data are renormalized to the lifetime-integrated X-ray flux data such that they have identical values at the 10th and 90th percentile of flux.

To determine whether the given CDFs in different physical parameter spaces, or for different subsamples, have statistically significant differences, we utilize the Anderson-Darling test (hereafter AD test) for two samples. The AD test was developed as an alternative to the Kolmogorov-Smirnov test. The AD test was designed to be sensitive to differences in the tails of two CDFs, making this test appropriate for our analysis of the photoevaporation desert, which is represented in the high flux tail. The Kolmogorov-Smirnov test is most sensitive to differences in the center of the distribution [Anderson and Darling, 1954]. Nevertheless, we confirm our results regarding statistical differences in the distributions with the Kolmogorov-Smirnov test and find consistent conclusions. We choose, however, to report results for the AD test, for the reasons cited above.

To compare the shape of the transition from the desert to the center of the planet distribution, we also consider the probability distribution function (PDF)—simply histograms of the planet distributions in flux space.

2.3 Results

2.3.1 Lifetime-integrated X-ray flux as a function of stellar mass

We examine the dependence of lifetime-integrated X-ray luminosity on stellar mass and age, to see in detail how host star properties can affect the propensity for a planet to photoevaporate. In Fig. 2.4, we use the results from the lookup table discussed in section 2.2.1

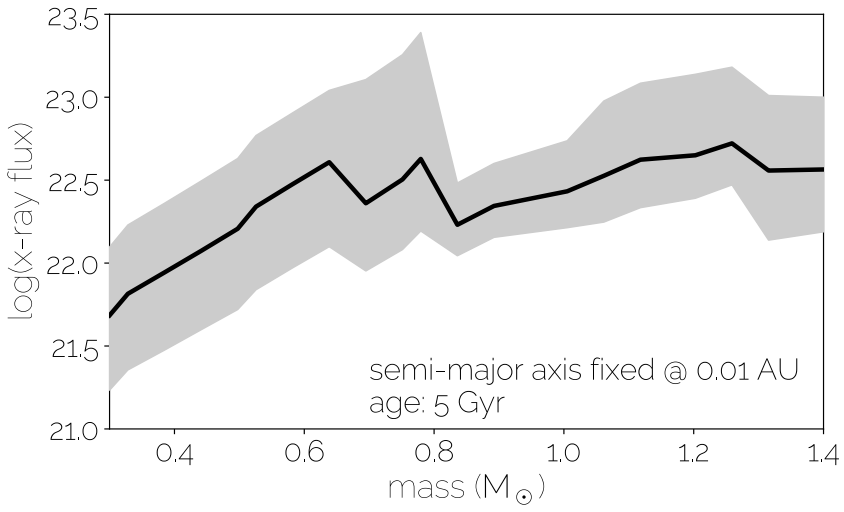

Figure 2.4: Integrated X-ray flux over a lifetime of 5 Gyr for a planet at 0.01 AU, as a function of stellar type. The shaded error bars denote 2σ errors calculated from a Monte Carlo sampling of the Jackson et al. [2012] and Shkolnik and Barman [2014] data.

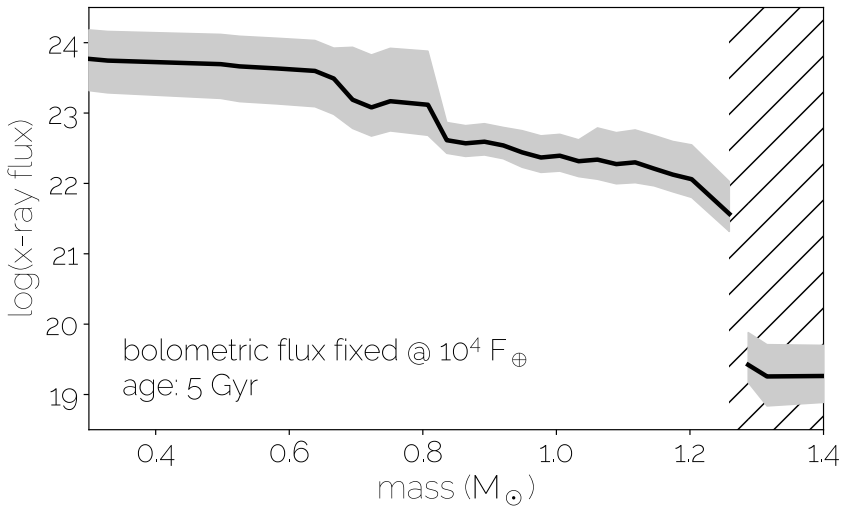

Figure 2.5: Integrated X-ray flux over a lifetime of 5 Gyr, for a planet with its 5 Gyr bolometric flux fixed at $10^4 F_\oplus$, as a function of stellar type. Note that the semi-major axis at which the planet is placed must be varied depending on the stellar type of the host star. The shaded error bars are calculated in the same manner as in Fig. 2.2. Stars within the hatched region have already left the main-sequence at an age of 5 Gyr.

to examine how the lifetime-integrated X-ray flux would vary as a function of stellar mass for a planet of age 5 Gyr fixed at a semi-major axis of 0.01 astronomical units (AU). The shaded error bars denote the 2σ error in the lifetime-integrated X-ray fluxes, as determined by our Markov Chain Monte Carlo fits to the X-ray data.

The lifetime-integrated X-ray flux increases as the stellar mass increases, which is not surprising given that the bolometric luminosity increases with mass. What is not quite as intuitive, is that the lifetime-integrated X-ray flux changes by only an order of magnitude for stars with $0.3 < M_{\odot} < 1.4$, despite the fact that the bolometric luminosity varies by two orders of magnitude over this mass range. Almost all of the drop in lifetime X-ray luminosity with lower stellar mass happens for the M-dwarfs $< 0.6\ M_{\odot}$. Above this mass, the lifetime X-ray luminosity is roughly flat with stellar mass since increases in the saturation level and lifetime (see Fig. 2.1) roughly balance out decreases in bolometric luminosity. Meanwhile below that mass, lifetime X-ray luminosities not only decrease as a function of mass, but also become strongly age-dependent even at several Gyr, likely due to their longer activity lifetimes combined with their continued bolometric luminosity evolution from Kelvin Helmholtz contraction (Fig. 2.4).

Fig. 2.5 further emphasizes the implications of the proportionally high X-ray luminosities of low-mass stars. In this plot we have fixed the present-day bolometric flux at $10^4\ F_{\oplus}$ for a planet of age 5 Gyr. In order to fix the bolometric flux, the semi-major axis of the planet must be varied for different stellar types. For a planet of age 5 Gyr, the lifetime-integrated X-ray flux is two orders of magnitude greater if it orbits a $0.3\ M_{\odot}$ star when compared to a star of mass $1.2\ M_{\odot}$. This plot provides an intuition for how a plot of the *Kepler* planets in radius vs. bolometric parameter space (e.g Fig. 2 of Lundkvist et al. [2016]) will be affected when the independent variable is changed to lifetime-integrated X-ray flux. For a plot calibrated to have the same parameter space in bolometric flux and lifetime-integrated X-ray flux (as we have done) for a solar mass star, all planets orbiting low-mass stars will move to higher lifetime-integrated X-ray fluxes relative to those emitted

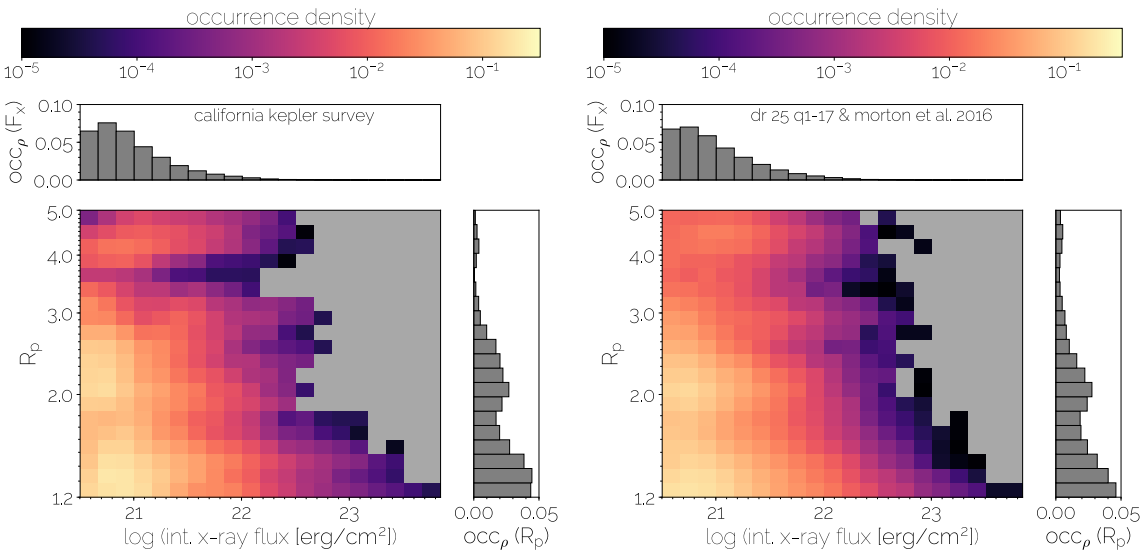

a) b)

Figure 2.6: a) Occurrence densities for the complete subsample of the California Kepler Survey. Summed occurrences over planet radius and integrated X-ray flux are shown in the 1D histograms along the plot edges, and use the same axes as the two dimensional occurrence plot. The grey shaded regions denote grid cells in which there are no data. b) The same plot, but for the complete subsample of the Q1-17 DR 25 and Morton et al. 2016 data. confirmed planets.

by a Sun-like star, while all planets orbiting high-mass stars will move to to lower lifetime-integrated X-ray fluxes. We predict that this shuffling of planets will change the shape of the planet distribution, as well as the shape of the photoevaporation desert.

The dramatic drop off in integrated X-ray flux for stellar masses greater than $M_\odot = 1.2$ in Fig. 2.5 is the result of these stars leaving the main sequence before 5 Gyr. When the stars leave the main sequence, their luminosity increases dramatically, necessitating the placement of the planet at comparatively long semi-major axes for the calculation of a bolometric flux at 5 Gyr of 10^4 $F_\oplus$. Combined with the fact that we stop time-integration of the host star's X-ray luminosity when it leaves the main sequence, the resultant time-integrated X-ray fluxes are lower by ~ 2 orders of magnitude compared to those stars that are still on the main sequence.

2.3.2 Comparison of the California Kepler Survey and Morton et al. 2016 and Q1-17 DR 25 dataset

The CKS sample has more precise stellar parameters, whereas the general Kepler Q1-17 DR 25 sample with planets confirmed by Morton et al. 2016 is larger. We use the CKS sample to evaluate the shape of the occurrence desert at higher precision for Sun-like stars, and use the Kepler Q1-17 DR 25 and Morton et al. 2016 sample to explore the desert as a function of stellar spectral type. In Fig. 2.6, we compare the calculated occurrences for the subsample of these datasets that we have chosen to be complete near the desert edge (see section 2.2.2). The purpose of this plot is to make note of systematic differences in the dataset that may affect our analyses. We note that in two dimensions, we consider the grid resolution of this plot to be oversampled in that many individual cells will have relative errors in occurrence greater than 10. We focus our attention on the occurrences summed over radius and lifetime-integrated X-ray flux (shown as histograms on the edges of the plot, with the same axes as the 2D plot). The bound of the plot on the low flux end has been set for the lifetime-integrated X-ray flux for a planet on a 10 day period, around a solar mass star with age of 5 Gyr, as a result of our completeness cut that eliminates all planets on greater than 10 day orbits. Any drop off in occurrence on the low flux end over the parameter space of interest is very likely the result of our period cut and we consider this to be nonphysical.

No systematic differences are apparent. In both datasets, the peak occurrence as a function of lifetime-integrated X-ray flux occurs at $\sim 10^{20.7}$ erg/cm^2. As a function of radius, the peak occurrence in the CKS data occurs at 1.3 $R_\oplus$, while the Q1-17 DR 25 and Morton et al. 2016 peaks at $R_\oplus$. Although reporting the occurrence density values in two dimensions is avoided due to our grid oversampling the parameter space as discussed in the previous paragraph, perhaps the most noticeable difference between the two datasets is visible just by considering relative variations in occurrence. The Q1-17 DR 25 and Morton et al. 2016 sample exhibits more smearing of occurrence densities across both dimensions,

while subtle variations that separate different planet populations are more important in the CKS data. This is a result of the factor of $\sim$2 – 3 greater uncertainties in the Q1-17 DR 25 and Morton et al. 2016 dataset. These uncertainties were discussed in section 2.2.2, and those with respect to R_p, and M_* are of particular consequence, with the latter having a large affect on the calculation of the lifetime-integrated X-ray flux. The splitting of the planet population by a "photoevaporation valley", or a local minimum of planet occurrence at $R_p = 1.7R_\oplus$ into two populations, one with peak occurrence at $R_p = 2.3R_\oplus$, and another with peak occurrence at $R_p = 1.3R_\oplus$ and at a higher value in the flux domain is consistent with the results of Fulton et al. [2017] (see their Fig. 10). Nevertheless, the valley is still apparent in the Q1-17 DR 25 and Morton et al. [2016] data set. The fact that it is still observable allows us to comment on its variation as a function of stellar type, which we will discuss in section 2.3.6.

2.3.3 Analyzing the photoevaporation desert in two dimensions

We now define the location of the photoevaporation desert, a region statistically consistent with no sub-Neptune sized planets at high irradation, possibly as a result of atmospheric photoevaporation stripping these planets down to rocky cores of size $< 1.4\ R_p$. In Fig. 2.7, we use the methodology described in section 2.2.3 to define the location of the photoevaporation desert in the CKS data. The hatched region in Fig. 2.7a defines a region of total occurrence consistent at the 2σ level with an occurrence of zero, in the parameter space of present-day bolometric flux and planet radius. This is the parameter space that most previous discussions of the photoevaporation desert in the data, e.g. Lundkvist et al. [2016] and Fulton et al. [2017] have used. In Fig. 2.7c the hatched region defines the photoevaporation desert (with the same criteria for occurrence) in the parameter space of lifetime-integrated X-ray flux. The bounds for both plots are chosen to be equivalent for a planet orbiting a solar mass star of age 5 Gyr. Fig. 2.7b and Fig. 2.7d show the relative errors in the occurrences of **Fig. 7a** and Fig. 2.7c respectively. The errors are smallest at the center of

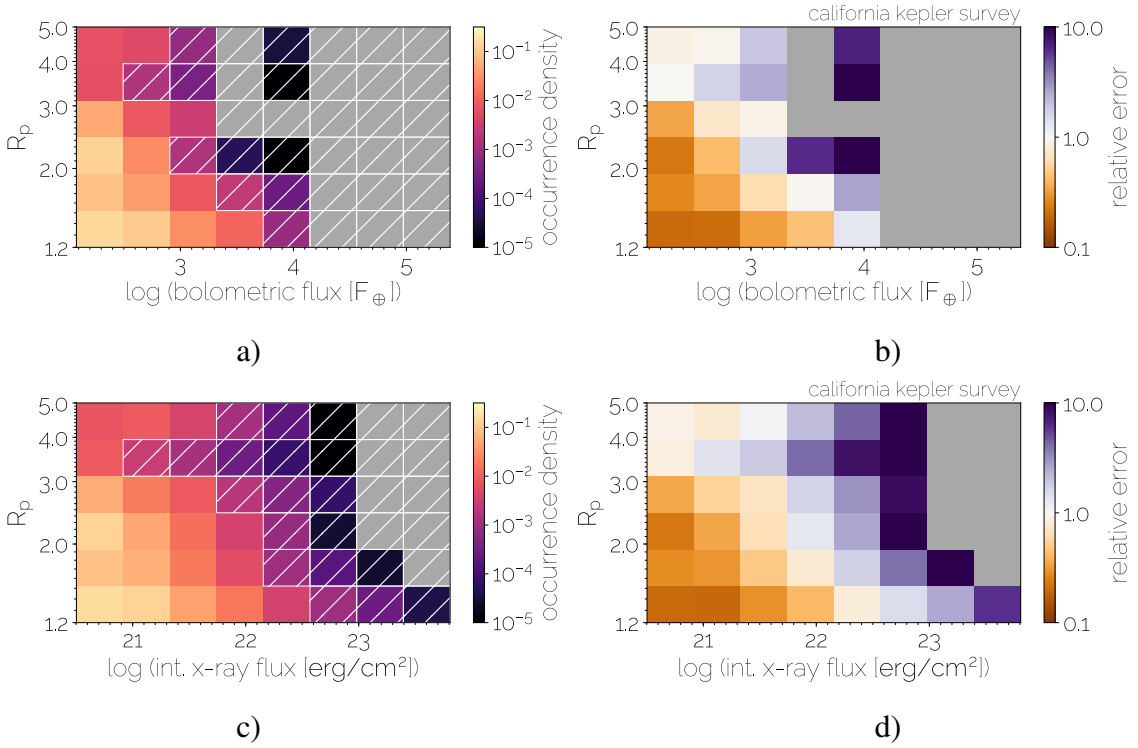

Figure 2.7: Occurrence densities for the complete subsample of the California Kepler Survey, specified on a grid for which the maximum relative error in a grid cell is ~ 10. The photoevaporation desert is shown as the hatched region and defined as an area consistent with zero planets at the 2σ level. Plots are for a) the present-day bolometric flux and c) the lifetime-integrated flux parameter spaces. The flux bounds of plots a) and c) are set to be equivalent for a solar mass star of age 5 Gyr. Plots b) and d) indicate the relative errors for the respective plots.

the planet distributions where large numbers of planets are found in each grid cell, and are greatest at the edges of the distribution, including the desert, where grid cells can consist of just several fractional planets

In both parameter spaces, the desert boundary has a negative slope in R_p vs flux. In bolometric flux, the highest flux value at which the desert boundary is drawn is 2.09 $\times 10^3 F_\oplus$ and located at a radius of 1.52 – 1.93 $R_\oplus$. The lowest flux at which the desert boundary is drawn 3.12 $\times 10^2 F_\oplus$, which is found at a radius of 3.11 – 3.94 $R_\oplus$. The highest and lowest fluxes for lifetime-integrated X-ray flux are found at the same two radii ranges, with values of 1.43 $\times 10^{22}$ erg/cm^2 and 8.23 10^{20} erg/cm^2 respectively. Despite the maximum and minimum fluxes of the desert boundaries occurring at the same radii, there are hints of differences in the shape of the desert between the two parameter spaces. In lifetime-integrated X-ray flux, the flux value at which the desert boundary is drawn appears to decrease monotonically as radius increases until a minimum at 3.1 – 3.9 $R_\oplus$, before increasing again. For bolometric flux, this same monotonic behavior is not found, with a concavity in the desert boundary at 2.4 – 3.1 $R_\oplus$. We note, however, that the shape of the drawn desert is sensitive to the errors of planet parameters, and more rigorous sensitivity testing would be required to make statistically significant claims on the differences in desert shape.

The radius and flux values that define the desert boundaries are recorded in Table 2.2. Comparisons of the desert we have found with other data sets will be made in section 2.4.1

Table 2.2: Photoevaporation desert boundaries as a function of planet radius.

Data set	Planet radius range					
	1.2 – 1.52	1.52 – 1.93	1.93 – 2.45	2.45 – 3.11	3.11 – 3.94	3.94 – 5.0
			Bolometric flux ($F_\oplus$)			
California Kepler Survey	5.41 $\times 10^3$	2.09 $\times 10^3$	8.07 $\times 10^2$	2.09 $\times 10^3$	3.12 $\times 10^2$	8.07 $\times 10^2$
			Life-int. X-ray flux (erg/cm^2)			
California Kepler Survey	3.70 $\times 10^{22}$	1.43 $\times 10^{22}$	1.43 $\times 10^{22}$	5.52 $\times 10^{21}$	8.23 $\times 10^{20}$	5.52 $\times 10^{21}$
Q1-17 DR 25 & Morton et al. 2016						
M & K subsample	1.50 $\times 10^{22}$	1.50 $\times 10^{22}$	1.50 $\times 10^{22}$	5.71 $\times 10^{21}$	2.18 $\times 10^{21}$	5.71 $\times 10^{21}$
G subsample	1.50 $\times 10^{22}$	1.50 $\times 10^{22}$	5.71 $\times 10^{21}$	2.18 $\times 10^{21}$	2.18 $\times 10^{21}$	5.71 $\times 10^{21}$
F subsample	2.18 $\times 10^{21}$	8.33 $\times 10^{20}$	3.18 $\times 10^{20}$	3.18 $\times 10^{20}$	3.18 $\times 10^{20}$	3.18 $\times 10^{20}$

2.3.4 The photoevaporation desert in one dimension: Cumulative distribution functions

We use cumulative distribution functions (CDFs) over the flux dimension, beginning with the highest fluxes, to examine the location of the photoevaporation desert, which is represented in the higher-flux portion of the CDF, as well as the shape of the photoevaporation desert, which is represented in the slope of the CDF. The shape of the photoevaporation desert is also represented in the probability density functions (PDFs) that we generate, which show variations in the probability density of planets as a function of flux. In Fig. 2.8a, we compare cumulative distribution functions (CDFs) of the gaseous and rocky planets in the CKS data set in the parameter space of lifetime-integrated X-ray flux. We have defined rocky to be planets with radii of 1.2 – 1.8 $R_\oplus$, and gaseous planets to be between 1.8 – 4 $R_\oplus$. The Anderson-Darling (AD) test on the two cumulative distribution functions returns an AD statistic of 9×10^3. Because this is much greater than the 1% critical value of 3.75, we consider the flux-dependent behavior of the rocky and gaseous planets to be different with 99% confidence.

In addition, both the CDF and PDF (Fig. 2.8b) show that the distribution of rocky planets is shifted to higher fluxes than the gaseous planets. The fact that there is an underdensity of high-flux gaseous planets, relative to rocky planets, is suggestive of a process shaping the gaseous planet population which is not affecting the rocky planets—namely photoevaporation.

In Fig. 2.9a the CDFs for our complete CKS sample are compared in the parameter spaces of bolometric flux and lifetime-integrated X-ray flux. To do this comparison, we renormalize the bolometric flux distribution to the 10^{th} and 90^{th} percentiles of the lifetime-integrated X-ray flux distribution (see section 2.2.3). The AD statistic of 444 is again larger than the 1% critical value of 3.75, indicating with 99% confidence that the distribution of planets in bolometric flux and lifetime-integrated X-ray flux are different. For the PDF in

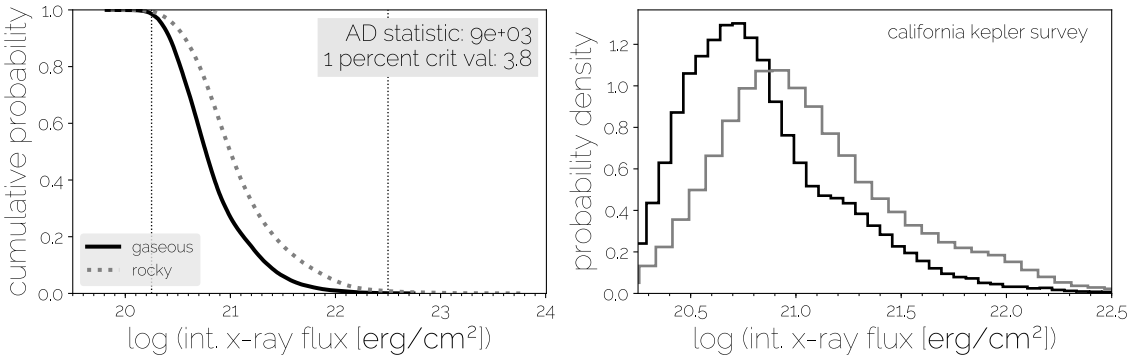

a) b)

Figure 2.8: a) A comparison of the cumulative distribution functions (CDF) for the rocky super-Earths and gaseous sub-Neptunes (which we define as between 1.2 – 1.8 $R_\oplus$, and 1.8 – 4 $R_\oplus$ respectively) in the complete subsample of the California Kepler Survey. The Anderson-Darling (AD) statistic comparing the two CDFs is shown. b) The probability distribution function (PDF), which indicates the onset of the desert location as well as the sharpness of the transition from the photoevaporation desert to the center of the planet distribution.

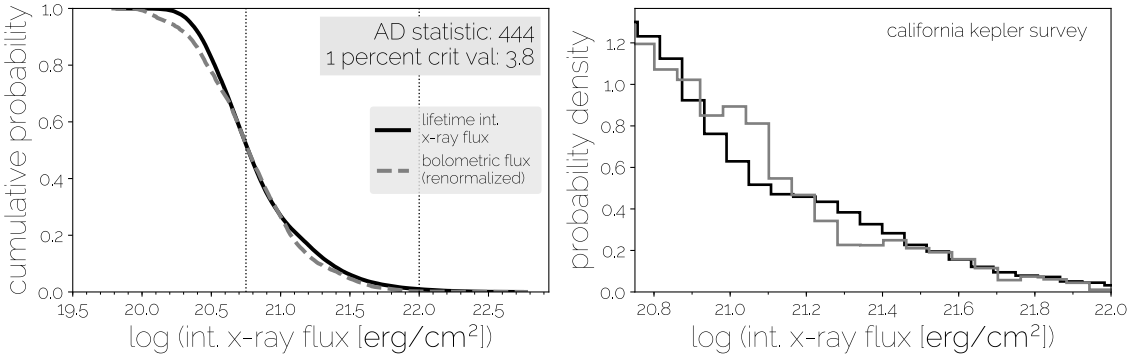

a) b)

Figure 2.9: a) The CDF of all sub-Neptune sized planets in the California Kepler Survey. We compare the CDFs of the planets in the parameter spaces of present-day bolometric flux and lifetime-integrated X-ray flux, and the AD statistic for this comparison is shown. For this comparison, the bolometric flux data are renormalized to the lifetime-integrated X-ray flux data such that they have identical values at the 10th and 90th percentile of flux. b) The PDF, containing the same information as described in Fig. 2.8b.

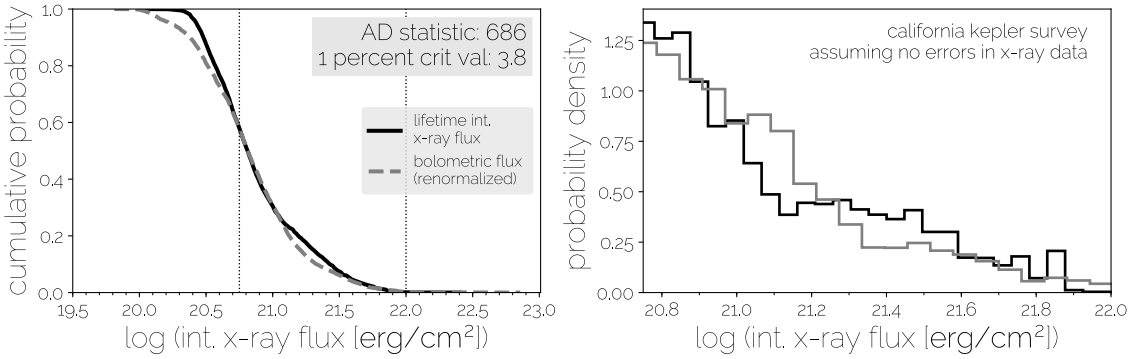

a) b)

Figure 2.10: a) The CDFs shown in Fig. 9, with the exception that for the lifetime-integrated X-ray calculation, the X-ray luminosities as a function of age and stellar mass are assumed to be known exactly. b) The PDF, containing the same information as described in Fig. 2.8b.

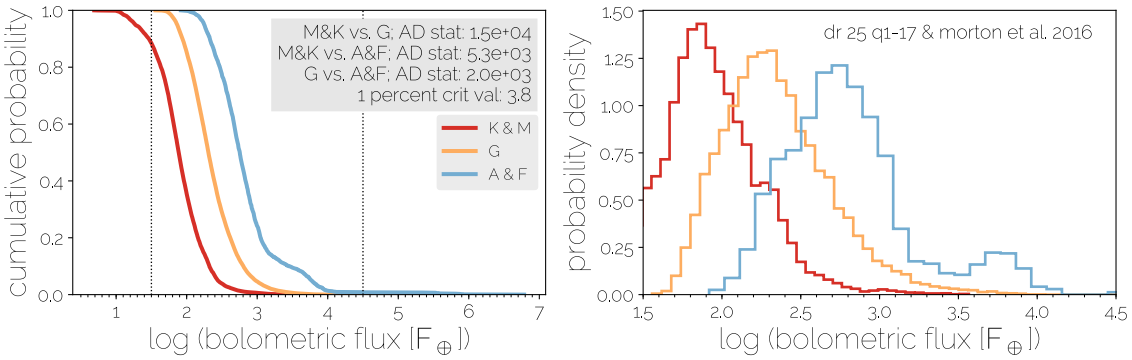

a) b)

Figure 2.11: a) The CDFs of all sub-Neptune sized planets as a function of stellar type for the complete Q1-17 DR 25 and Morton et al. [2016] subsample in the bolometric flux parameter space, as well as the AD statistics comparing each CDF. b) The PDF, containing the same information as described in Fig. 2.8b.

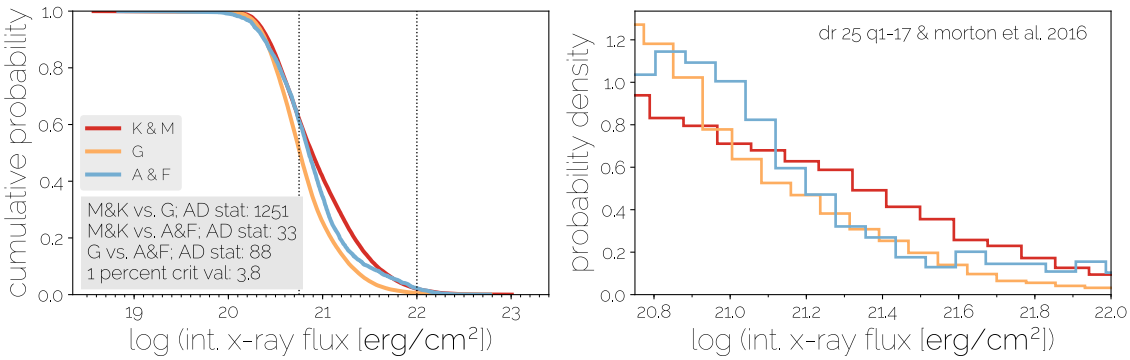

a) b)

Figure 2.12: a) The CDFs of all sub-Neptune sized planets as a function of stellar type for the complete Q1-17 DR 25 and Morton et al. [2016] subsample in the lifetime-integrated X-ray flux parameter space, as well as the AD statistics comparing each CDF. b) The PDF, containing the same information as described in Fig. 2.8b.

Fig. 2.9b, one curve does not exhibit consistently steeper slopes than the other, with the exception of some small underdensities and overdensities in the bolometric flux distribution. By casting the photoevaporation desert in a parameter space directly tied to the physical process of photoevaporation, lifetime-integrated X-ray flux, one might expect the desert to be more sharply defined when compared to the bolometric flux parameter space. Nevertheless, the CKS sample consists of largely Sun-like stars, and accounting for differences in stellar type is the biggest reason why lifetime integrated X-ray flux should produce a sharper desert edge compared to bolometric flux—an effect that would not be dramatic in this sample. In section 2.3.5, we will examine the CDFs for the DR 25 Q1-17 and Morton et al. 2016 dataset, which encompass a wider variety of stellar types.

We consider the possibility that a steeper CDF for the lifetime-integrated X-ray flux is not apparent due to the errors in the X-ray observations. Fig. 2.10 shows the same CDF comparison of Fig. 2.9, with the exception that the X-ray luminosity is assumed to be known exactly as a function of stellar mass and age (e.g. Fig. 2.2, but with relative errors of 0 across the entire parameter space). Although the AD statistic for the two distributions again indicates that the distributions are distinct, once again neither the slope of the CDF for lifetime-integrated X-ray flux nor the slope of the CDF for bolometric flux is consistently

greater than the other. Assuming there are no systematic errors in the X-ray observations of Jackson et al. [2012] and Shkolnik and Barman [2014], which seem unlikely given that their relations are largely in agreement with theoretical considerations, the steepness of the slopes for the sub-Neptune planet distribution in lifetime-integrated X-ray flux space and bolometric flux space appear to be largely indistinguishable.

2.3.5 The desert as a function of stellar type

We now examine differences in the photoevaporation desert as a function of stellar type. Examining the desert for a variety of stellar types is insightful because bolometric flux varies by close to 2 orders of magnitude among FGK stars, but the lifetime x-ray luminosity is roughly flat with stellar mass for $M_* > 0.6\ M_\odot$.

Fig. 2.11 compares the CDFs for the different stellar types as a function of bolometric flux, using the subsample of the DR 25 Q1-17 and Morton et al. 2016 dataset, chosen to be complete near the desert edge. In the CDFs (Fig. 2.11a) as well as the PDFs (Fig. 2.11b), it is clear that the distributions of the planets around different stellar types peak at different fluxes. The AD statistics are all $> 10^3$, indicating that all distributions are significantly distinct from one another.

Fig. 2.12 compares the CDFs for the different stellar types using the same sample, but in the lifetime-integrated X-ray flux parameter space. The similarity among the distributions in lifetime X-ray flux compared to bolometric flux (Fig. 2.11) is immediately apparent. All three distributions peak around $10^{20.7}$ erg/cm^2. Although the AD statistic indicates that all distributions are still distinct from one another, the AD statistics in lifetime X-ray flux are 1 – 2 dex lower than in bolometric flux. This suggests that the primary reason for differences in the distributions as a function of stellar type are a result of bolometric flux variations as well as variations in the L_X/L_{bol} ratio as a function of stellar type. When the planet distribution is cast into lifetime-integrated X-ray flux, the parameter physically tied to the evaporation process, the bulk of the variability among stellar types

is corrected for. The differences that remain are possibly due to non-steady-state X-ray emissions (flares and coronal mass ejections) that are not measured in the X-ray data, as well as other secondary processes. Another possiblity is variations in data precision as a function of stellar type—wherein uncertainties for late stellar types typically have slightly larger average uncertainties.

The difference between the M & K and G type CDFs (AD statistic = 1251) is found to be considerably greater than between the M & K and A & F samples (AD stat. = 33), or between the G and A & F samples (AD stat. = 88). In comparing the PDFs (Fig. 2.12b), the larger difference between the CDFs for the M & K and G type stars is apparent in a sharper transition for the G-type stars between the desert and the center of the planet distribution—starting out at high fluxes with the smallest planet probability density, until transitioning to the highest planet probability density at the median flux.

Fig. 2.13 compares the stellar types in the radius dimension in addition to the flux dimension. The consistency in the location of the desert among the sample of M & K type stars (Fig. 2.13a) and G type stars (Fig. 2.13c) in lifetime-integrated X-ray flux is visible. The desert drawn for the F type stars is significantly larger than for either the M & K or G samples. However, we note that the number of planets in the F sample is considerably smaller than in the other samples (fractional planets equivalent to a total of 6.2 planets, compared with 52.9 for the M & K sample, and 97.4 for the G sample, see Table 2.1). For this reason, the errors in the desert boundaries drawn for the F sample will be much larger than for the other samples—this could very possibly be the reason for the difference in the shape of the drawn desert region for the F-type stars in two dimensions.

2.3.6 The photoevaporation valley as a function of stellar type

We now examine the photoevaporation valley, the gap in the *Kepler* planet data at 1.5 – 2 $R_\oplus$ first reported by Fulton et al. 2017, using the same stellar subsamples of section 2.3.5. The photoevaporation valley occupies a distinct parameter space from the photoevaporation

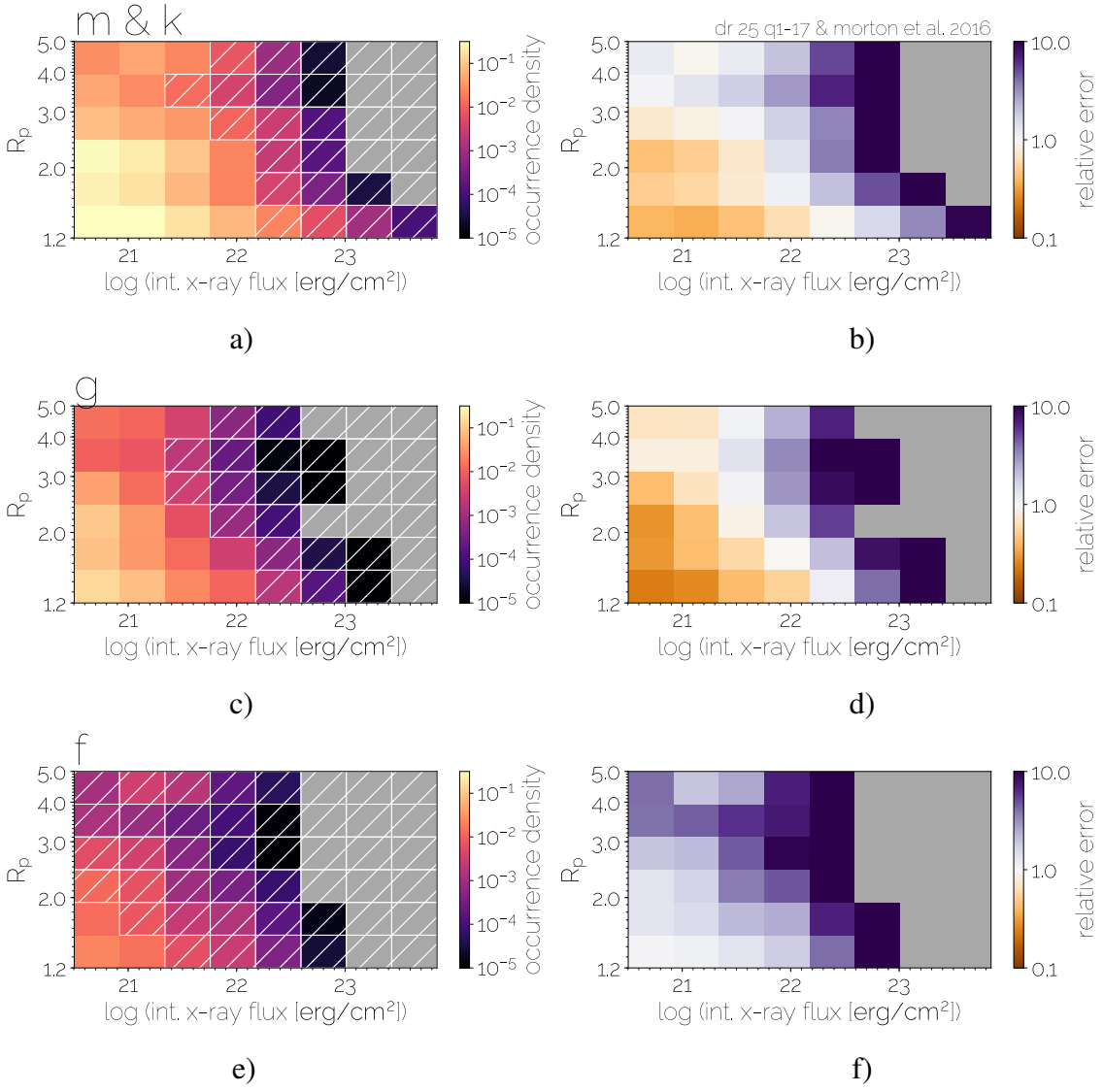

Figure 2.13: Changes in planet occurrence and the shape of the photoevaporation desert as a function of stellar type for the complete Q1-17 DR 25 and Morton et al. [2016] subsample. a) M & K type stars c) G type stars e) F type stars. The relative errors for the above subsamples are shown in subplots b), d) and f) respectively. The plotting conventions are the same as for Fig. 2.7

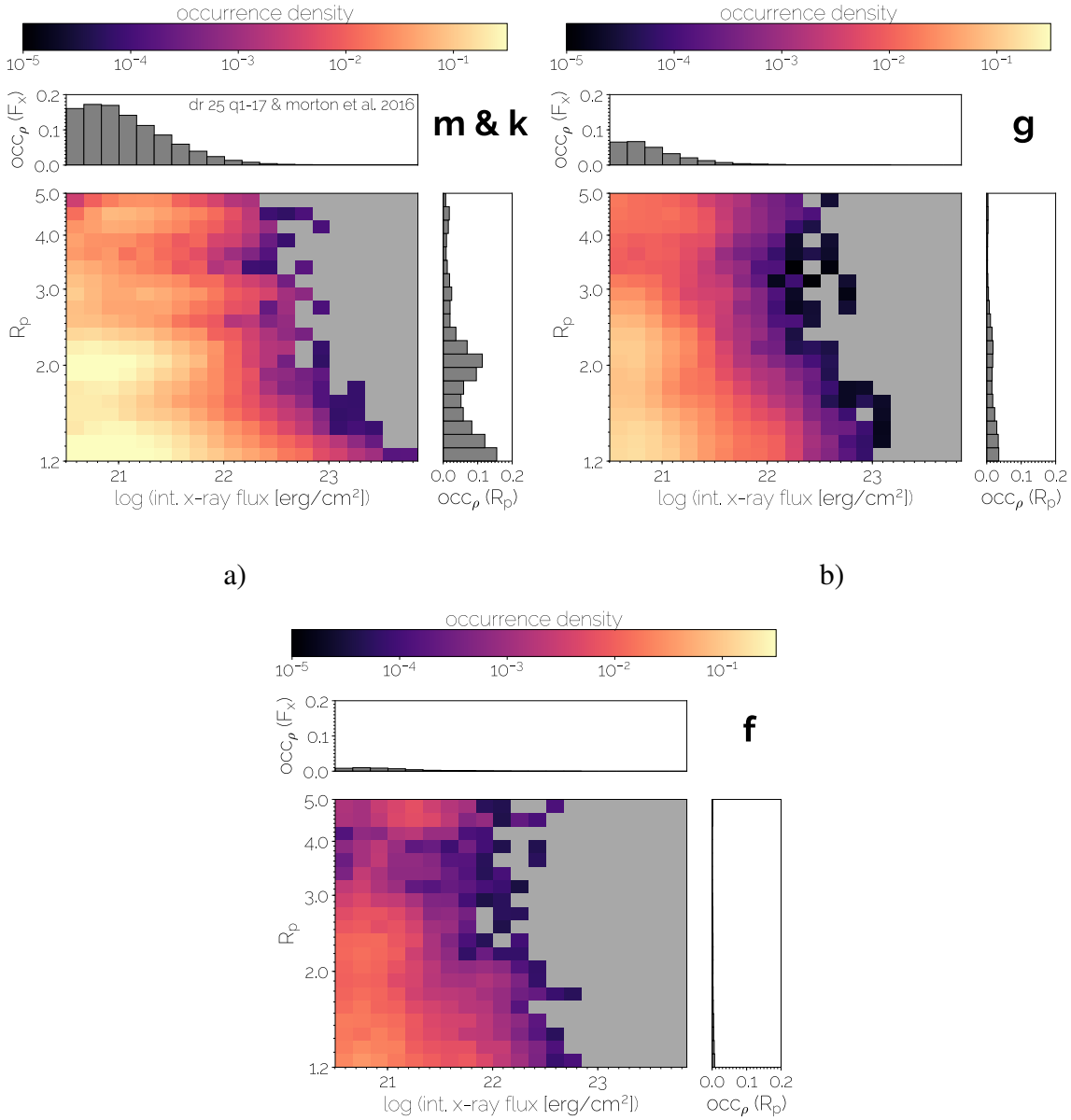

Figure 2.14: Summed 1D occurrences over planet radius and lifetime-integrated X-ray flux, as a function of stellar type. a) M & K type stars b) G type stars c) F type stars. The plotting conventions are the same as for Fig. 2.6

desert, and for a visual comparison the reader is referred to Fig. 10 of Fulton et al. [2017]. We now look at the samples at a finer grid resolution in Fig. 2.14 so as to investigate in detail the occurrences summed over the radius and integrated X-ray flux dimensions. Although the parameter space is now oversampled in two dimensions, the relative errors for the occurrences for the M &K and G-type stars in one dimension (over radius and flux space, visible as the 1D histograms on the axes of the plots) are still less than our criteria of < 1 dex. The valley is clearly visible in the right panel of Fig. 2.14a, which consists of the M & K type star subsample, as a minimum in occurrence at $R_p = 1.7R_\oplus$. This represents an advance to studies of the photoevaporation valley in a suggestion of its presence for later stars; the original discovery of Fulton et al. 2017 reported the valley for solar-type stars hotter than ~ 4600 K.

In Fig. 2.15 we show these same occurrence densities marginalized as a function of radius, with the distributions now normalized to probability densities, facilitating comparisons among stellar types, as well as with 1 σ error bars (calculated using equation 2.2). The M & K radius distribution is indicative of a valley at $R_p = 1.6\oplus$ at the 1 σ level. The valley is not apparent in the G sample, and cannot be reported on at the 1 σ level for the F type stars.

2.4 Discussion

2.4.1 Comparison of our photoevaporation desert with previous studies

The desert we defined in section 2.3.3 is in good agreement with previous theoretical studies. The slope of our desert boundary drawn in is qualitatively consistent with the slope of the theoretical curve presented in Fig. 7 of Owen and Wu 2013, with the intercept of our boundary in lifetime-integrated X-ray flux offset by roughly a half order of magnitude to higher fluxes. Although Owen and Wu 2013 made a visual comparison of their theoretical curves with a previous *Kepler* table, our having defined a desert boundary directly from the data using statistical considerations allows for direct quantitative comparisons with evapo-

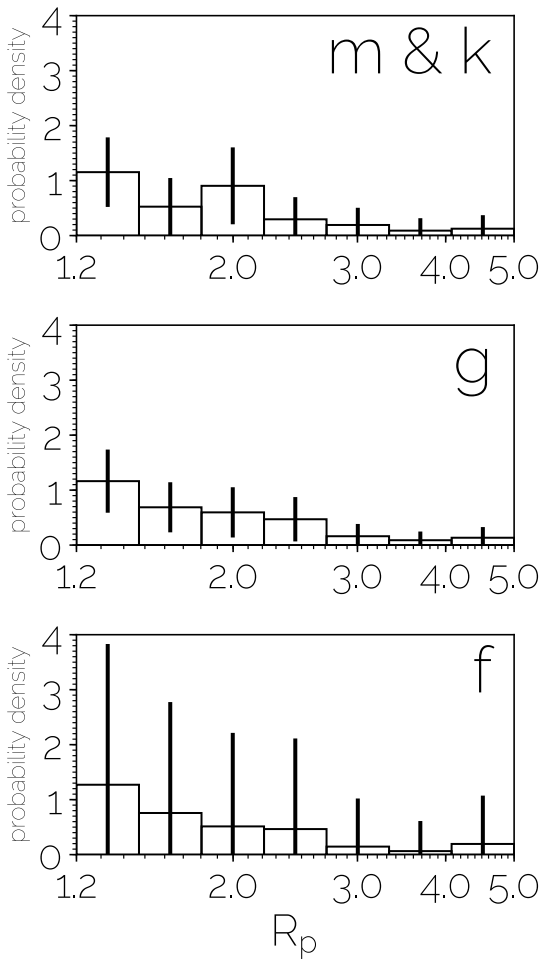

Figure 2.15: Histograms comparing the relative occurrence densities of planets as a function of radius among stellar types. The lines denote 1 σ error bars.

ration models.

In the parameter space of bolometric flux, the desert region identified by Lundkvist et al. [2016] can be considered a subset of the desert we have drawn. However, rather than try to define a region completely absent of planets, we have shown that a much larger portion of the parameter space spanning lifetime-integrated X-ray fluxes from 8.23 $\times 10^{20}$ to 10^{24} erg/cm^2 (see Table 2.2 for tabulations of the desert boundary) can be considered consistent with zero planets at the 2 σ level.

2.4.2 Evidence that the gaseous planets are sculpted by photoevaporation, a depletion in gaseous planets at high lifetime integrated X-ray fluxes, and implications for habitability

Our finding of the center of the planet distribution for gaseous planets ($1.8 < R_\oplus < 4$) occuring at lower lifetime-integrated X-ray fluxes compared to rocky planets ($1.2 < R_\oplus < 1.8$) may be indicative of the distribution of gaseous planets as a function of lifetime-integrated X-ray flux being shaped by the photoevaporation process. Similarly, it suggests a depletion in gaseous compared to rocky planets at higher fluxes.

We find that the utility of examining the photoevaporation desert in the lifetime-integrated X-ray flux parameter space is most pronounced when looking at a sample of planets orbiting a large variety of stellar types. This is apparent in the transition of the stellar subsamples from bolometric flux space in Fig. 2.11, where the distributions peak at different fluxes, to lifetime X-ray flux where the stellar subsamples pile up (Fig. 2.12). The 1 – 2 dex drop in the AD statistics after this transition are indicative of variations in bolometric flux and the L_X/L_{bol} ratio as a function of stellar type being the number one source of variation in the planet distributions of sub-Neptunes. When these variations are corrected for and the sub-Neptunes are examined in lifetime X-ray flux space, we are left with a sample more resembling a single distribution. We consider these photoevaporative considerations to be the primary candidate for shaping our observed planet distributions as a function of stellar types, as dynamical considersations which also vary as a function of stellar type

(e.g. tidal loss) take place at considerably shorter orbital periods (e.g. several hours for Sun-like stars) than even the tails of our planet distributions. In considering differences among stellar types, the fact that M-dwarfs emit proportionaly more of their flux in X-rays (Fig. 2.1) means that planets in the inner edge of the habitable zone around mid to late M-dwarfs receive considerably more high-energy radiation fluxes than would be the case for planets around the inner edge of the habitable zone around a sun-like star. In fact, the inner edge of the habitable zone overlaps with the defined photoevaporation desert. Thus, the presented evidence for photoevaporation sculpting atmospheric evolution also suggests that the photoevaporation process may place a new inner bound on the habitable zone for planets around mid to late M-dwarfs, based on where a planet can retain its atmosphere.

In addition, evidence for the photoevaporation process shaping the distribution of sub-Neptunes has implications for finding the frequency of Earth-sized rocky planets in the habitable zones of Sun-like stars (termed $\eta_{\oplus}$). If a significant fraction of planets slightly larger than Earth and with higher irradiation are the evaporated cores of sub-Neptunes, this represents a fundamentally different formation process from Earth itself (which could not have formed from photoevaporation of a gaseous planet, Owen and Mohanty 2016), and studies that use these planets in determining $\eta_{\oplus}$ will overestimate this parameter [Lopez and Rice, 2016].

2.4.3 Differences in the desert among stellar types: Flares and coronal mass ejections as well as predictions for future surveys of M dwarfs

After correcting for the bolometric variations among stellar types using lifetime-integrated steady-state X-ray fluxes, whatever variations that remain among stellar types could possibly be a result of secondary X-ray emissions from flares and coronal mass ejections, processes that are also expected to vary as a function of stellar type. Although obvious physical signatures of these processes are not apparent in our results, we suggest that our approach of accounting for steady-state X-ray emissions when examining the photoevaporation desert,

coupled with higher precision measurements of late-type stars using a methodology similar to that of the California Kepler Survey, could place observational constraints on the importance of these secondary X-ray emission sources on the photoevaporation process. Furthermore, despite the variety of stellar types present in the Q1-17 DR 25 *Kepler* catalog, the lowest mass stars are still early M dwarfs, whereas massive increases in flaring activity begin with mid M-dwarfs later than M3. Current and future surveys will discover many more planets around mid M dwarfs. These include the *K2* mission, the *Transiting Exoplanet Survey Satellite* (*TESS*), the *Planetary Transits and Oscillations of stars* (*PLATO*) mission, as well as the Characterizing Exoplanets Satellite (*CHEOPS*). The addition of the planets discovered by these missions, in combination with our method of correcting for steady-state X-ray emissions, could evaluate the significance of flaring in contributing to the photoevaporation process.

2.4.4 The photoevaporation valley for late type stars

Our findings are suggestive at the 1σ level of a photoevaporation valley for the M & K dwarfs, centered at $\sim 1.6R_{\oplus}$. Thus the valley may not be unique to Sun-type stars, and higher precision measurements of late-type stars should allow for rigorous claims on its dependence on stellar type. Our suggestion that the photoevaporation valley continues for planets around for M & K dwarfs motivates such follow-up measurements, which in turn may allow for interpretation of the origins for the photoevaporation valley—whether it be planet core luminosity driving atmospheric loss [Ginzburg et al., 2017] or the same photoevaporation process responsible for the photoevaporation desert [Owen and Wu, 2017].

2.5 Summary

We have examined how lifetime-integrated X-ray flux varies as a function of stellar mass and age. This knowledge was used to cast the *Kepler* dataset into the lifetime-integrated X-ray flux parameter space where statistical constraints were placed on the photoevaporation

desert, as well as the photoevaporation valley for late type stars. The key results of this study are summarized below.

(i) Lifetime-integrated X-ray luminosity decreases with stellar mass, and almost all of this drop happens for M-dwarfs $< 0.6\ M_{\odot}$. Above this mass, the lifetime X-ray luminosity is roughly flat with stellar mass since increases in the saturation level and lifetime

(ii) For a given present day insolation, planets around lower mass stars experience relatively more X-ray flux over their lifetimes ($\sim$100 $\times$ more for a planet orbiting a 0.3 $M_{\odot}$ star versus 1.2 $M_{\odot}$).

(iii) We have defined a photoevaporation desert, a region consistent with a planet occurrence of zero at the 2 σ level. The highest lifetime X-ray flux at which the desert boundary is drawn is 1.43 $\times 10^{22}\ erg/cm^2$ and located at a radius of 1.52 – 1.93 $R_{\oplus}$. The lowest lifetime X-ray flux at which the desert boundary is drawn is 8.23 $\times 10^{20}$ erg/cm^2, which is found at a radius of 3.11 – 3.94 $R_{\oplus}$.

(iv) We find that the flux-dependent behavior of rocky and gaseous planets are different with 99% confidence. We observe that the the distribution of rocky planets is shifted to higher fluxes than the gaseous planets, suggestive of a process shaping the highly irradiated gaseous planet population which is not affecting the rocky planets (which we interpet as photoevaporation).

(v) The utility of examining the photoevaporation desert in the lifetime-integrated X-ray flux parameter space is most pronounced when looking at a sample of planets orbiting a large variety of stellar types. The probability density functions of the sub-Neptunes peak at different bolometric fluxes for different stellar types. Correcting for steady-state stellar X-ray fluxes by casting the sub-Neptune sample in lifetime-integrated X-ray flux space, the planets around all stellar types more closely resemble a single distribution.

(vi) Our findings are suggestive at the 1σ level of a photoevaporation valley for the M & K dwarfs, centered at $\sim 1.6 R_{\oplus}$.

We have not only place improved observational constraints on the location of the photo-

evaporation desert, but have also developed a methodology to correct for how steady-state X-ray emissions shape the sub-Neptune population as a function of stellar type. We suggest that this technique, combined with the greatly increased sample size of planets around low-mass stars that will be made available by current and future surveys, will be valuable in isolating the effects that secondary X-ray emission sources such as flares and coronal mass ejections have on the photoevaporative process.

CHAPTER 3

MODELING TRANSMISSION WINDOWS IN TITAN'S LOWER TROPOSPHERE: IMPLICATIONS FOR INFRARED SPECTROMETERS ABOARD FUTURE AERIAL AND SURFACE MISSIONS

Published in modified form as:

G.D. McDonald*, P.M. Corlies*, A.G. Hayes, J.J. Wray, M. Ádámkovics, M.J. Malaska, M.L. Cable, J.D. Hofgartner, S. Hörst, L.R. Liuzzo, J.J. Buffo, R.D. Lorenz, E. Turtle (Submitted), Modeling transmission windows in Titan's lower troposphere: Implications for infrared spectrometers aboard future aerial and surface missions. *authors contributed equally.

3.1 Introduction

Titan's atmosphere consists of an opaque combination of methane (1.5% – 5.6%) and other higher order hydrocarbons, which acts to absorb much of the incident insolation in the near-IR [Kuiper, 1944, Flasar et al., 2005, Niemann et al., 2010]. The result of this for spectral studies of Titan's surface in the infrared is spectral windowing—from the top of the atmosphere, Titan's surface can only be studied at a handful of methane transmission windows (referred to hereon simply as windows) [McCord et al., 2008].

The Visual and Infrared Mapping Spectrometer (VIMS) aboard the Cassini mission has been used to put constraints on Titan's surface composition through the measurement of reflected sunlight within these windows. There are eight atmospheric windows in VIMS's 0.85-5.17 μm (micron) infrared channel, centered at: 0.94, 1.08, 1.28, 1.6, 2.0, 2.7, 2.8 and 5 μm [Soderblom et al., 2010], which can be seen as areas of greater than $\sim 50\%$ transmission in Fig. 3.2. The narrow width of the windows has largely precluded hyperspectral observations within them, which would allow for the detection of specific surface

compounds through the identification of absorption bands at unique wavelengths. The exceptions are the reported detections of ethane in the south polar Ontario Lacus [Brown et al., 2008] and of benzene and possibly cyanoacetylene [Clark et al., 2010].

Because of the spectral windowing resulting from methane absorption, classification of Titan's surface to date has largely consisted of "multispectral" analysis, relying primarily on integrated spectral averages in each of the windows to look for spectral slopes, temporal variations, and relative changes between the windows. This form of analysis has lead to the identification of a few spectrally distinct terrain types on Titan, including the "5 micron bright," "dark blue" and "dark brown" regions, which are inferred to vary in their relative content of water ice vs organic compounds. [Barnes et al., 2005, 2008, Soderblom et al., 2007, Solomonidou et al., 2014, MacKenzie and Barnes, 2016]. Additional measurements of the surface composition include near-surface visible and near-infrared spectra taken by the Descent Imager/Spectral Radiometer (DISR) aboard Huygens which has been interpreted as evidence for water ice and yellow tholins [Tomasko et al., 2005]. In-situ measurements by the Huygens Gas Chromatograph Mass Spectrometer (GCMS) indicated methane moisture in the ground, the detection of ethane, and possibly cyanogen, acetylene and carbon dioxide [Niemann et al., 2010]. Finally, measurements of the loss tangents of the polar lakes and seas using the RADAR altimeter suggest tertiary compositions of primarily methane, ethane and nitrogen [Mastrogiuseppe and Poggiali, 2014, Mitchell et al., 2015, Mastrogiuseppe et al., 2018]. Despite this large set of measurements, robust detections of surface compounds are restricted to the simplest aliphatic and aromatic hydrocarbons: methane, ethane and benzene. The primary constituents of the majority of Titan's surface remain unknown, limiting our understanding of the geologic processes operating on Titan's surface, the ends products of its photochemistry as well its potential for prebiotic chemistry.

Due to the narrowness of the windows previously discussed, the majority of open questions concerning Titan's surface composition cannot be answered using existing data alone

and will require a future mission. In this manuscript, we will discuss the severity of the transmission of Titan's atmosphere insofar as it influences observations of Titan's surface in the near to mid-IR. Through modeling of Titan's atmosphere at different altitudes we will discuss improvements that should be considered in future mission concepts in order to maximize the scientific return of these missions. We also quantify the degree to which additional light sources, such as an infrared lamp, can facilitate the use of these widened windows. Finally, we evaluate the utility of these windows for hyperspectral detections of compounds relevant for characterizing Titan's surface geologic and chemical processes.

3.2 Methods

3.2.1 Radiative Transfer Model

Titan's atmosphere is modelled using PyDISORT, a plane parallel radiative transfer model, with a pseudo-spherical correction built around the discrete ordinates method [Ádámkovics and Mitchell, 2016]. Measurements from the Huygens probe determine the atmospheric structure , composition, and scattering properties of aerosols (for multiple scattering) in Titan's atmosphere [Niemann et al., 2010]. Gas opacities are calculated through correlated k-coefficients generated from line-by-line calculations of line assignments from the newly updated HITRAN2016 database [Gordon et al., 2017]. Given the incompleteness of the HITRAN2016 database at shorter wavelengths, we restrict our analysis to those > 0.8 μm. At these wavelengths, the contribution from Rayleigh scattering by gas molecules is also small and as such is not included in the model.

Structure

To assess the variation in transmission with altitude, Titan's atmosphere is divided into a minimum of 100 layers. These layers are linearly spaced in altitude, covering the range from the surface to the nominal mission altitude of interest. For the orbiter case, we limit this range to that sampled by the Huygen's probe (below 147 km). Linear spacing in altitude

is used for uniform altitude sampling, but has no significant impact on derived values. Values for the temperature, pressure, and densities as measured by the Huygens probe [Niemann et al., 2010] are then interpolated to the model layers. For ease of calculation, all viewing geometries are assumed to be at a zero degree incidence and emission angle (zero phase). Thus, we simulate scenarios similar to observing at equatorial latitudes near solstice. Therefore, the results that follow are a best case scenario, as significant increase in the phase angle would increase the path length through Titan's atmosphere, increasing the effects of both absorption and scattering through the atmosphere.

Aerosols

Aerosol scattering phase functions were measured with the DISR instrument on the Huygen's probe over the range from .8 μm – 5.2 μm for above and below 80 km [Tomasko et al., 2008]. Here, we extrapolate the values measured above 80 km down to the surface following the prescription of [Campargue et al., 2012], which they find to better match VIMS observations. Measurements provided in [Tomasko et al., 2008] are fit with a 32 order Legendre polynomial and are linearly interpolated to intermediate wavelengths.

Aerosol extinction was also measured by DISR and found to follow a power law distribution for wavelengths between 400 nm and 1600 nm [Tomasko et al., 2008]. Total extinction curves were measured for three regions: $<$30 km, 50 km – 80 km, and $>$ 80 km. Within the lowest two regions, uniform vertical opacity is used for each. Above 80 km a scale height of 65 km is used [Tomasko et al., 2008].

Values for the aerosol extinction and scattering phase functions were only measured over limited wavelength ranges. For the extinction, the power laws defined in [Tomasko et al., 2008] are extrapolated to the wavelengths out to 10 μm. Previous use of this extrapolation has shown reasonable agreement with observations out to 5 μm [Griffith et al., 2012]. For the scattering phase function, the values measured for the longest wavelength (5.166 μm) are simply extrapolated to 10 μm. Because the aerosol properties are so poorly

constrained (even at shorter wavelengths) a more complicated extrapolation cannot be motivated. A uniform single scattering albedo of ω = 0.96 is used for all wavelengths. The extrapolation of these parameters and the assumptions used are all smoothly varying (or constant) values and therefore offer no significant contribution to the shape of the spectral windows, which are dominated by gas absorption. Therefore, although more complicated applications may be used, they should not significantly affect the conclusions of this work, which concern the spectral shape of Titan's windows.

Composition and Opacity

Included in the model are N_2, H_2, CH_4, CH_3D, C_2H_2, C_2H_6, and CO abundances as measured by the GCMS instrument on the Huygen's probe from an altitude of 147 km down to Titan's surface [Niemann et al., 2010]. Methane was measured directly by the GCMS instrument and was found to follow a saturation curve in Titan's troposphere down to $\sim$ 7km, where the mole fraction remains constant to the surface at $\sim$5.7%. The CH_3D/CH_4 ratio is set to the value of 2×10^{-4} as measured with CIRS [Nixon et al., 2012]. H_2, C_2H_6, and C_2H_2 were also measured with the GCMS and found to be constant with altitude with mole fractions of 1×10^{-3}, 1×10^{-5}, and 1×10^{-6} respectively [Niemann et al., 2010].

Opacities are calculated using high resolution (0.001 cm^{-1}) line-by-line calculations to properly resolve the line shape of each of the methane assignments. Absorption spectra are generated for a grid of temperatures and pressures relevant to Titan conditions—the grid is then used to generate correlated-*k* coefficients at a nominal resolution of 2 cm^{-1}. Pressure and Doppler broadening effects are modelled through a Voigt profile, in combination with a far wing correction factor as described in De Bergh et al. 2012. We note that these correction factors have been modelled only for the 1.6 μm window, but have been found to generally agree with the other methane windows < 5 μm [Hirtzig et al., 2013], with only a small correction for the 2.0 μm window. Here, we do not apply the additional correction at the 2.0 μm window, as high precision model fitting to observational data is not the goal of

this work. Due to a lack of observations to further constrain the far wing line behaviour at longer wavelengths, we apply the same cutoffs to wavelengths > 5 μm.

Collision-induced absorptions (CIAs), resulting from the deformation of colliding non-polar molecules, are important in Titan's atmosphere for N_2–N_2 and N_2–H_2 collisions. These affect in particular the structure of the 2 μm window, the 2.7 μm and 2.9 μm doublet, and the blue side of the 5 μm window. Absorption coefficients for the CIAs measured at Titan relevant conditions (97.5K) are taken from McKellar 1989.

The final component of the atmosphere is the parameterization of the surface scattering. In this work, we assume a lambertian surface scattering with a grey albedo of 0.1 for all wavelengths. Although we know the spectral variation of Titan's surface within the narrows windows available from orbit, the albedo outside of these regions (over much of the near-IR) is still unknown. Therefore, we opt for the simple model of a grey scattering surface for this work. This allows us to focus primarily on the effects of the atmosphere on observations of the surface.

3.2.2 Surface compounds of interest

Our chief interest is in using the widened atmospheric windows available in the lower atmosphere for studies of Titan's surface composition. We have therefore compiled absorptions of chemical species of interest for geologic, chemical and potential prebiotic processes operating on Titan's surface. These compounds span a range of different functional groups, consisting of inorganics, hydrocarbons, nitriles, amides/amino acids and nucleobases. The strongest absorption minima for these species were identified using the National Institute of Advanced Industrial Science and Technology (AIST)'s Spectral Database for Organic Compounds (SDBS). Absorption minima were selected based on their transmission being $\lesssim 30\%$ through the KBr (potassium bromide) disks as prepared by SDBS.

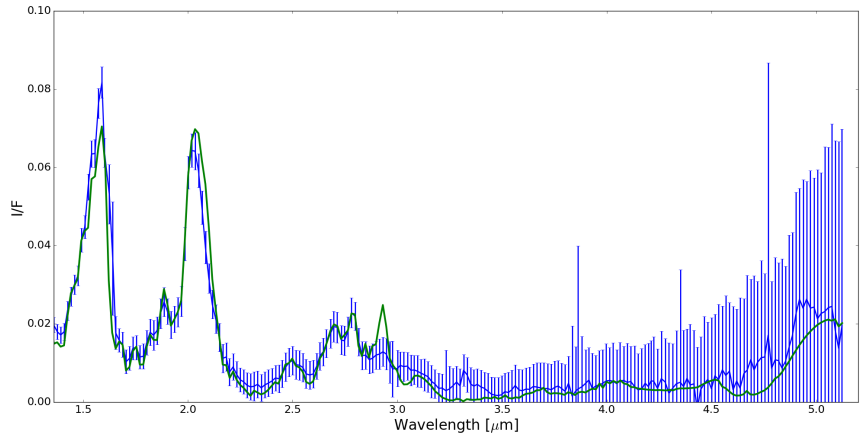

Figure 3.1: A comparison of the albedo produced by the PyDISORT model (green) with VIMS observations and errors (blue) for the Huygens landing site.

3.3 Results

3.3.1 Model accuracy

In order to assess the accuracy of the model, a modeled albedo spectrum is compared with a VIMS spectrum for the Huygens landing site in Fig. 3.1. The model albedo fits the VIMS observation (using the physical parameters measured by Huygens for the landing site and without adjustment) within error at the majority of wavelengths, with exceptions at 2.1 – 2.2 μm, 2.9 – 3.0 μm and 3.35 - 3.5 μm.

3.3.2 Transmission vs Altitude

With the model established, we calculate the direct transmission through Titan's atmosphere as a result of absorption from the various gases. Fig. 3.2 plots the expected transmission for four characteristic mission altitudes: lander, drone, balloon, and orbiter. We find strong, but narrow absorptions from each of the trace gases, some in areas of particularly clear methane absorption. In these cases, such as for CO and C_2H_2 at 5 μm, these narrow absorptions help to define the cutoffs of various windows in Titan's near-IR spectrum.

Methane acts as the primary absorber in Titan's atmosphere and generates most of the features observed in Titan's near-IR reflectance. We find that most wavelengths, besides those that are transparent from orbit, remain relatively opaque unless close to the surface, demonstrating that only a reduction in the integrated column of methane can improve the near-IR visibility of Titan's surface. Only at altitudes less than $\sim$1 km is there any appreciable change in the effects from methane absorption. For example, the 5 μm window is broadened by a factor of only $\sim$10% relative to orbit at an altitude of 3 km, but this broadening increases to $\sim$25%, $\sim$75%, and $\sim$175% for altitudes of 1 km, 100 m, and 10 m, respectively (see Table 3.1 for reported window widths based on percent transmission). The 5 μm case is the most dramatic broadening of Titan's windows, but demonstrates the need for future missions to operate as low as possible in Titan's atmosphere in order to improve our knowledge of possible surface compositions.

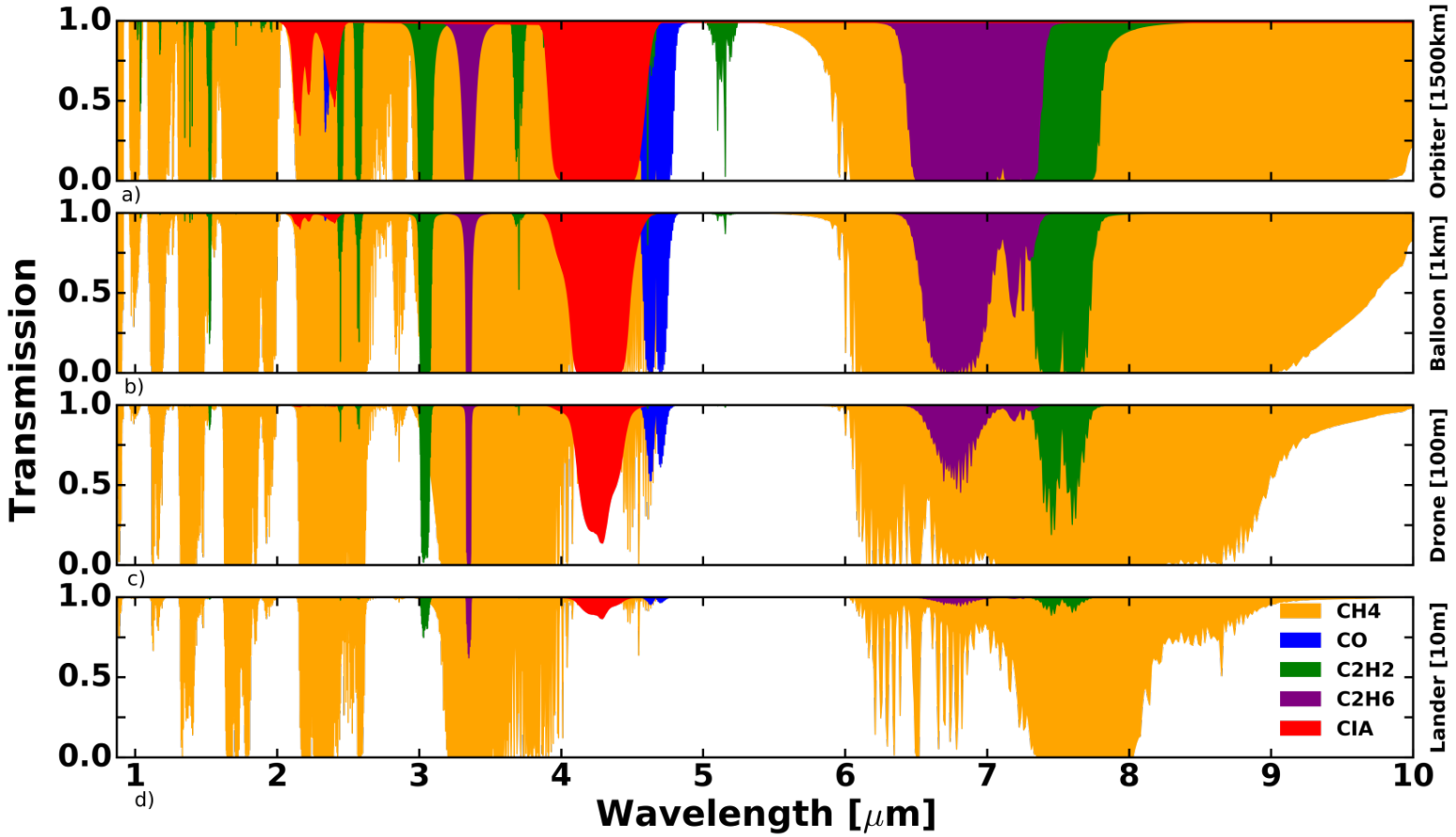

Figure 3.2: The gaseous absorption in Titan's atmosphere for four different nominal mission architectures: orbiter, balloon, drone, and lander. White areas indicate spectral regions with signal above zero percent. Methane (orange) is the primary absorber in Titan's atmosphere. From orbit, only very narrow band windows are found that can see through to Titan's surface. The 5 μm window is the widest and most transparent. As the mission altitude decreases, absorption in the windows decreases and the wings of the windows widen to allow for greater spectral coverage. By the time one reaches the surface, most of Titan's near-IR spectrum is observable, barring a few narrow regions of exceptionally strong methane absorption.

Table 3.1: Spectral windows defined based on 90% or 10% transmission through the relevant distance to the surface.

Trans.	Window ranges (μm)								
Orbit (1500 km)									
90%	0.92 - 0.96	1.04 - 1.09	1.28 - 1.30	2.00 - 2.06	2.78 - 2.80	4.82 - 5.06	5.23 - 5.68		
10%	0.92 - 0.97	1.03 - 1.11	1.22 - 1.30	1.98 - 2.13	2.68 - 2.96	4.78 - 5.95	9.96 - 10.0		
Balloon (3 km)									
90%	0.92 - 0.96	1.04 - 1.09	1.25 - 1.30	1.57 - 1.60	1.99 - 2.09	2.78 - 2.80	2.92 - 2.94	4.80 - 5.85	
10%	0.91 - 1.12	1.21 - 1.31	1.49 - 1.62	1.87 - 1.90	1.97 - 2.14	2.78 -2.99	4.75 - 6.04	9.69 - 10.0	
Drone (100m)									
90%	0.90 - 1.12	1.20 - 1.31	1.49 - 1.62	1.88 - 1.91	1.95 - 2.14	2.64 - 2.99	4.75 - 6.03	9.60 - 10.0	
10%	0.87 - 1.34	1.42 - 1.63	1.81 - 2.16	2.62 - 3.14	3.96 - 6.14	6.55 - 6.60	8.52 - 10.0		
Lander (10m)									
90%	0.87 - 1.34	1.42 - 1.63	1.81 - 2.17	2.62 - 3.02	3.07 - 3.13	3.96 - 4.19	4.32 - 6.10	6.40 - 6.43	6.55 - 6.60	8.70 - 10.0
10%	0.87 - 2.27	2.4 - 3.02	3.60 - 7.31	8.07 - 10.0					

3.3.3 Expected Signal: Passive vs Active Illumination

Although transmission can be improved depending on mission altitude, it still does not mean that these spectral regions are immediately accessible. This is because passive solar illumination must pass through Titan's opaque atmosphere. Fig. 3.3 shows spectra of Titan's albedo at two altitudes in the atmosphere, comparing the differences between passive (solar) and active (lamp) illumination. Because the one way integrated column density through the entirety of Titan's atmosphere is large, solar illumination is mostly absorbed before it reaches the surface. Only in the transparent windows can it provide appreciable signal at the surface. However, if a mission were to include an active light source, such as a broadband lamp or LEDs, then the integrated column density from source to detector is simply the two way distance between the spacecraft and the surface. This is significantly shorter than the one way transmission through the atmosphere, and thus allows for a broader region of Titan's near-IR spectrum to be sampled before the light is absorbed. We note, however, that unless the windows have widened appreciably with respect to those observed from orbit (compare Fig. 3.3a to Fig. 3.3b), use of a lamp will not necessarily increase spectral coverage.

For an altitude with widened windows, onboard illumination is therefore required to access these spectral regions on a future in-situ mission to Titan. But there are several types of possible illumination sources. Fig. 3.3b plots a comparison between broadband and narrowband (LED) light sources. A broadband source offers the benefit of wide spectral coverage, but at the cost of significant power. LEDs much more efficiently emit in narrowband regions, however, it can be seen that for the wider spectral regions, particularly $>$ 2.7 μm, multiple LEDs are required to provide comparable coverage to a single broadband source (see **Fig 2b**). LEDs are also less efficient at longer wavelengths, and thus begin to require more power in this region. Short of 2.7 μm, although the windows do broaden significantly, they are still narrow enough such that a single, tuned LED can cover the entire spectral window. We note that the exact spectral coverage of an LED and its ability

to provide sufficient illumination will depend on both its temperature and power. We define the available regions in Fig. 3.3b from commercial LEDs (typically power of a couple mW), limiting their spectral coverage to regions of 80% peak spectral density. However, the exact signal-to-noise ratio (SNR) that can be obtained in these regions will depend on the number and power of LEDs as well as their angular distribution (which would dictate how concentrated their light is). We do not model SNRs here given that they are highly dependent on the properties of spectrometer instrument suites (telescope size, detector, integration times etc.). However, given an LED's ability to concentrate power within narrow spectral regions, they act as a viable low-energy, counterpart to broadband illumination for narrow regions of interest. Thus, a probable mission architecture in the future could include a combination of LED sources for shorter wavelengths and a broadband source for longer wavelengths, each of which can be selected depending on the observations being made.

3.3.4 Ability to detect surface compounds

Potential surface compounds of interest that could be detected in the widened spectral windows in the lower atmosphere range from biologically relevant to inorganic compounds. Fig. 3.4 shows the spectral windows available from altitudes relevant for future balloon (for which a distance of 3 km is used), drone (100 m) and lander (10 m) mission architectures. The windows are defined as regions where the atmospheric transmission is between 90% (minimum width) and 10% (maximum width). The absorption minima for a selection of surface compounds of potential interest are also shown, with the different subpanels showing compounds of different types. The absorption minima for the surface compounds that are plotted are also tabulated in Table 3.2.

Fig. 3.4a indicates the absorption minima of amides and amino acids. Only two compounds, urea and sarcosine, have absorptions that lie within spectral windows available from orbit (the 2.8 μm and redward edge of the 5 μm window that is not covered by the VIMS detector for urea, and the 2.8 μm window for sarcosine). Nevertheless, these ab-

sorptions lie in regions of low ($\sim 10\%$) transmission. The significant widening of the 5 μm window for a drone observing from distances of 100 m makes the detection of all listed compounds (glycine, L-alanine, sarcosine, β-alanine and 4-aminobutyric acid) a possibility. In addition, two absorption minima for urea (2.901 and 5.942 μm) now lie within windows. The ability to identify a compound based on two absorption minima, as for urea in this case, would significantly increase confidence in its purported detection. Observing from distances of 10 m places absorption features of additional amino acids (glycine and β-alanine) in wide enough spectral windows of high transmission that would likely enable true hyperspectral observations.

The ability to detect nucleobases and potential alternative nucleobases is examined in Fig. 3.4b. Although multiple species have absorption features in the 5 μm window from orbit (although at wavelengths redder than the 5.2 μm limit of the VIMS detector), it is only at 3 km or better where the features fall within areas of higher transmission. For example, observing from distances of 100 m places multiple cytosine absorption minima in window regions of high transmission, facilitating the possibility for robust detection. In addition, from 100 m all other species now have one absorption feature in regions of high transmission.

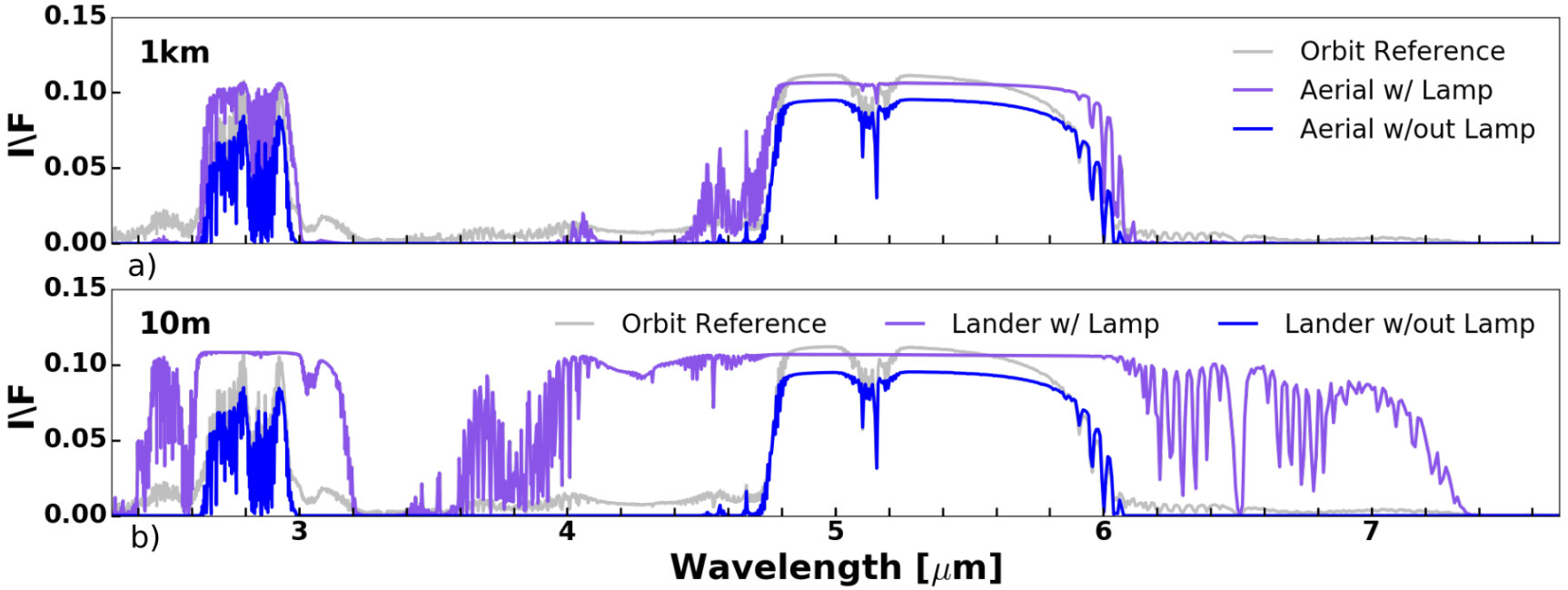

Figure 3.3: Comparison of Titan's simulated albedo between passive and active illumination at two different nominal altitudes. The orbital reference albedo (grey) matches closely to the "without lamp" cases (blue) because of the significant one-way opacity of Titan's atmosphere that effectively acts to extinct all incident solar light, except for in the windows. The orbit reference albedo is typically higher than the nominal mission case because of contributions from scattering in the upper atmosphere. a) comparison at 1km. With onboard illumination (purple) only a modest improvement is observed in spectral coverage on the wings of each window, suggesting a maximum mission altitude with which to obtain greater spectral coverage over an orbiter. b) comparison at 10 m. Significant enhancement in the spectrum is observed, with window broadening as high as $\sim$200%. Low altitude missions then, are favored for major improvements in spectral coverage in the near-IR. In this panel, shaded regions demonstrating typical coverage available form commercial LEDs are also indicated. See the text in section 3.3.3 for a more detailed discussion of using LEDs as a source of active illumination. Because of this spectral broadening, several LED's are required to cover the entire windows in the mid-IR, i.e. we define 4 LED bands in the 5 μm window and have only covered $\sim$50% of the entire window.

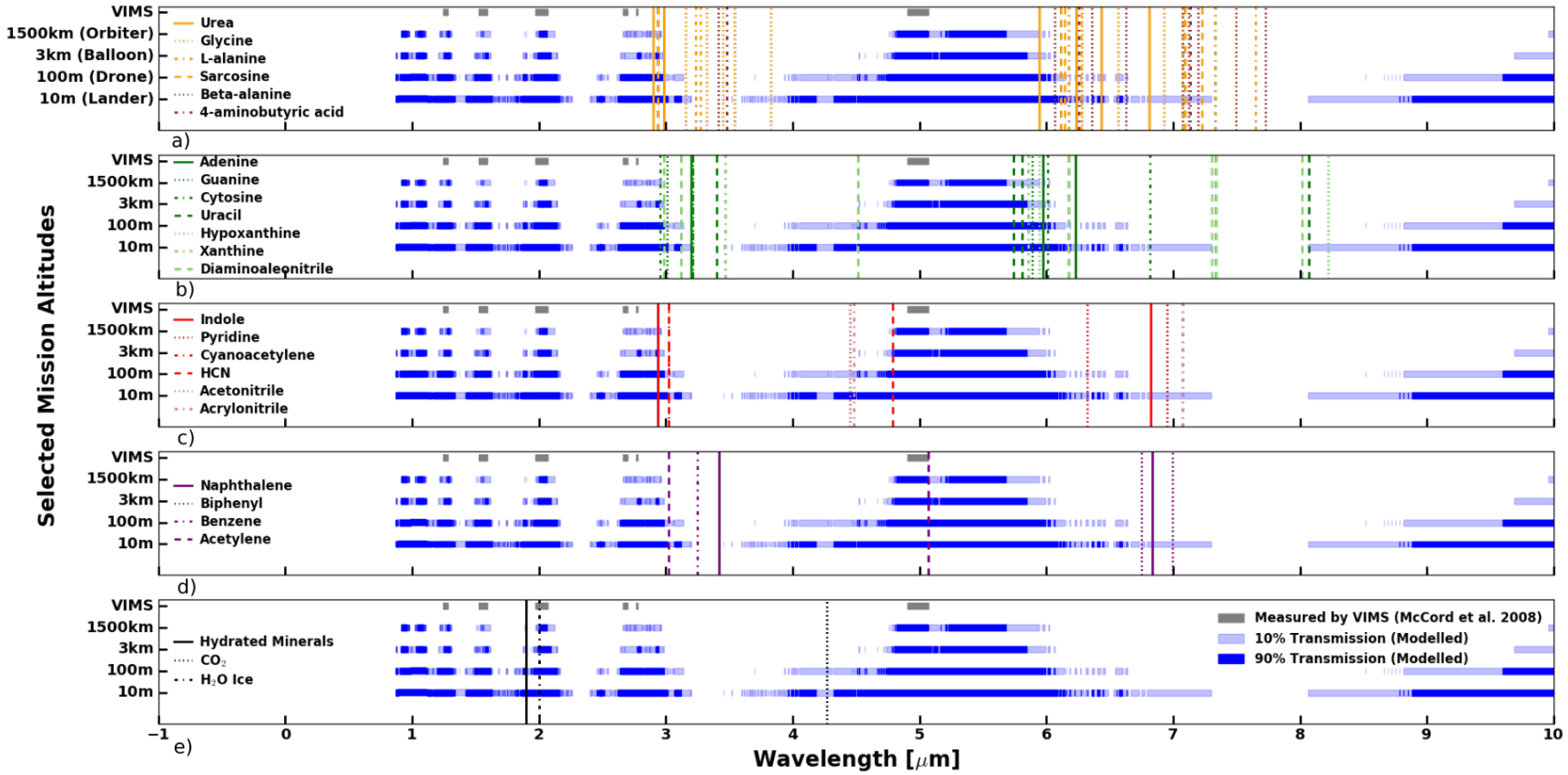

Figure 3.4: The spectral windows available from orbit as defined by McCord et al. 2008 for VIMS, as modeled from orbit (1500 km), and at altitudes relevant for future balloon (3 km), drone (100 m) and lander (10 m) mission architectures. The windows are defined using the horizontal shaded boxes as regions where the atmospheric transmission is between 90% (minimum width) and 10% (maximum width). The vertical lines denote major absorption minima for surface compounds of geological, chemical or prebiotic interest. The subpanels are divided based on the types of potential surface compounds shown: a) Amino acids/amides b) nucleobases c) nitriles d) hydrocarbons e) inorganics.

Fig. 3.4c demonstrates the prospect of detecting nitriles within the newly widened windows. The prospect for detection of nitriles within the windows, as shown in Fig. 3.4c, is now discussed. From orbit, only single absorption minima of indole and HCN fall within the transmission windows, albeit at the window edges and in areas of low transmission. Although propsects for detection of indole improve at 3 km, it is not until distances of $\sim$100 m that the 2.94 μm indole and 4.72 μm HCN absorption minima fall comfortably within areas of high transmission in the widened windows. Again from 100 m, a 3.02 μm feature shared by HCN, cyanoacetylene, acetonitrile and acrylonitrile falls in a window region of lower transmission. From a distance of 10 m, this feature falls into an area of higher transmission, in addition to a $\sim$ 4.45 μm acetonitrile and acrylonitrile absorption feature.

For hydrocarbons, shown in Fig. 3.4d, only absorption minima for benzene and acetylene, at 5.05 and 5.07 μm respectively, fall within a window from orbit. For distances of 100 m, a second acetylene absorption minimum at 3.02 μm can be observed and improves for a distance of 10 m. At distances of 10 m, naphthalene and biphenyl now have absorption minima in a window region with low transmission between 6.75-7.0 μm.

The absorption minima for inorganics are shown in Fig. 3.4e. From orbit, only water ice has an absorption minimum within a window at 1.9 μm. Observations improve significantly by 100m, allowing for absorption features of hydrated minerals and CO_2 to fall in regions of high transmission. The situation for 10 m observations is largely unchanged from 100 m.

Table 3.2: Absorption minima for species of geologic, chemical, and prebiotic interest.

Species	Absorption minima (μm)									
Amides/Amino Acids										
Urea	2.901	2.988	5.942	6.431	6.238	6.812				
Glycine	3.158	3.324	3.451	3.539	3.827	6.281	6.566	6.925	7.077	7.496
L-alanine	3.239	3.271	6.173	6.274	7.077	7.331	7.651			
Sarcosine	2.935	6.112	6.143	7.092	7.225					
Beta-alanine	3.413	6.068	6.357	6.627	7.077	7.123	7.194	7.496	7.728	
4-amino butyric acid	3.479	6.254	7.133							
Nucleobases										
Adenine	3.202	5.977	6.231							
Guanine	3.01	3.209	5.89							
Cytosine	2.956	6.013	6.817							
Uracil	3.209	3.403	5.741	5.811	5.974	8.071				
Hypo-xanthine	5.945	8.224								
Xanthine	3.469	5.858								
Diamino-aleonitrile	2.987	3.118	4.515	6.173	7.305	7.337	8.013			
Nitriles										
Indole	2.939	6.8213								
Pyridine	6.325	6.954								
Cyano-acetylene	3.02									
HCN	3.02	4.79								
Acetonitrile	4.45									
Acrylonitrile	4.484	7.077								
Hydrocarbons										
Naphthalene	3.418	6.835								
Biphenyl	3.418	6.752	6.993							
Benzene	3.25	5.05								
Acetylene	3.02	5.07								
Inorganics										
Hydrated Minerals	1.9									
CO_2	4.27									
H_2O Ice	2.0									

3.4 Discussion

We now consider questions in Titan surface and atmospheric science that could be addressed through the identification of compounds in these wider windows. The bulk composition of Titan's surface remains unknown. Identifying water ice vs benzene, acetylene or simple nitrile compounds such as indole as major surface constituents would have implications for the geologic processes operating on Titan's surface. For example, karstic evolution has been proposed as a formation mechanism for Titan's polar lakes, but requires a surface material that is soluble in liquid hydrocarbon [Hayes et al., 2008, Michaelides et al., 2016]. Testing this formation model ultimately requires that this surface material is identified. Further, candidate cryovolcanic features have been identified, including the 1 km high mountain adjacent to a $\sim$1.5 km deep depression at Sotra Facula [Lopes et al., 2013]. The observation of hydrated silicates around these features could be indicative of communication with Titan's interior and strengthen the case for their cryovolcanic origin. The ability to discriminate between hydrated silicates and pure water ice is only possible with broader spectral windows at low altitudes.

The identification of specific compounds on the surface can also inform our understanding of Titan's photochemistry. An area of debate has been whether aromatic rings are fused (forming polyaromatic hydrocarbons) or linked (forming phenyls) during transport in Titan's atmosphere [Delitsky and McKay, 2010]. Comparing the relative abundance of biphenyl and naphtalene (which may be possible from distances of 10 m) would be a major step in elucidating the dominant synthesis pathways for aromatic compounds on Titan.

Further information on the surface composition is also essential for characterizing the potential prebiotic chemistry occurring on Titan's surface. Laboratory studies of reactions between tholins and liquid water indicate that essential prebiotic building blocks including urea and amino acids can form [Khare et al., 1986, Nguyen et al., 2007, Raulin, 2008] over timescales relevant for impact melt events [Neish et al., 2008, 2009]. Such impactors

would likely also carry a variety of amino acids themselves [Burton et al., 2012]. We have demonstrated that the widened spectral windows available in the lower atmosphere could help confirm that these processes are occurring, as discussed in section 3.3.4.

Furthermore, Jeilani et al. 2015 have proposed mechanisms by which urea, along with acetylene sourced from Titan's atmosphere, can form pyrimidine nucleobases. However, whether such biologically relevant compounds are actually forming on Titan's surface, what specific ones are being formed, as well as their abundances remain open questions. The ability to identify uracil from distances of 3 km, as well as a host of other nucleobases from distances of 100 m or less (see Fig. 3.4b, in addition to the building blocks urea and acetylene being visible in the windows), would help address these questions.

Finally, recent studies using molecular simulations suggest that nitrile compounds, such as acrylonitrile, measured in situ in Titan's upper atmosphere [Vuitton et al., 2007], may form membranes and vesicles (termed "azotosomes") that could provide the function that liposomes do for biological organisms on Earth [Stevenson et al., 2015]. An important step towards assessing whether such azotosomes exist on Titan is confirming that these nitrile compounds also exist on the surface, and are not altered during transport through the atmosphere. We have shown that acrylonitrile may be detected from 100 m, and could comfortably be detected hyperspectrally from 10 m.

Although the Huygens DISR instrument used active illumination in the lower atmosphere to study the surface composition, the majority of major absorption minima for organic compounds of interest discussed above lie at wavelengths greater than $\sim$2.8 μm, significantly redder than the 0.8 – 1.8 μm wavelength range of Huygens. Only a future mission with much broader spectral coverage could detect these compounds.

3.5 Conclusions

In summary:

- We have demonstrated that the infrared spectral windows in the wavelength range 0.8

– 10 μm broaden considerably within the context of infrared spectrometers operating on missions in the lower atmosphere.

- Onboard illumination is required in order to observe the widened windows in the lower atmosphere. This is because the availability of solar radiation is largely restricted to within the windows available from orbit.

- Enhanced spectral coverage will provide profound insight into Titan's history and evolution and its potential to act as a biologically viable environment.

Future missions have been proposed for Titan [Lorenz, 2008, Sotin et al., 2011, Barnes et al., 2012, Stofan et al., 2013, Sotin et al., 2017] and will continue to be planned into the future [Turtle et al., 2017]. Studying Titan's surface composition is an explicit goal of all of these missions—our quantification of the widened spectral windows will assist in designing instruments for future low-altitude missions.

CHAPTER 4
CONCLUSION

4.1 Results

The contents of this thesis have demonstrated through two examples that a detailed understanding of the radiative occurring in a planet's atmosphere can provide constraints on its habitability.

In understanding the population of sub-Neptune sized exoplanets, I have shown indications that the lifetime-integrated X-ray flux is an important control on the population—consistent across host stars of different stellar types. This is suggetive of atmospheric photoevaporation driven by the host star's X-ray and extreme ultraviolet radiation sculpting the population of close-in sub-Neptunes. This process is known to be relevant for planets in the inner edge of the traditional habitable zone around late M dwarfs. The results presented herein thus strengthen the case that such planets would be completely stripped of their primordial H/He atmospheres, limiting both their ability to hold volatiles such as water as well as maintain surface pressures that would allow for surface liquids. This would in effect place a new boundary for the inner edge of the habitabile zone based on a planet's ability to retain an atmosphere.

Another example included concerns study of Titan, which possesses many of the criteria thought to be important for a planetary body to be habitable—a wealth of organic material produced from atmospheric photochemistry, a subsurface liquid water ocean, and energy from sunlight, possible cryovolcanic processes or impacts. However the ability to study Titan's potentital for prebiotic surface chemistry has been severlely limited by its thick and absorptive atmosphere that renders much of the infared useless for compositional studies from orbit. The detailed radiative transfer modeling of Titan's atmosphere presented

herein has shown what wavelengths would be available to, and in turn what compounds of chenmical and prebiotic relevance, could be detected by future missions operating within Titan's atmosphere. Our finding that many amides, amino acids and nucleobases could be detected from distances of several hundred meters makes a strong case that a future mission in Titan's lower atmosphere could determine whether complex prebiotic chemistry is indeed occurring on Titan's surface.

4.2 Future work

Understanding the effects of photoevaporation on the sub-Neptune population, as well as its impact on the habitability of planets in the inner edge of the traditionally defined habitable zone around M dwarfs will continue to be an important area of study. The discovery and radii characterization of additional planets around mid M-dwarfs will aid in extending the stellar mass range over which the photoevaporation desert is identified (in the parameter space of lifetime-integrated X-ray flux and planet radius). These characterizations will be made possible by the *Kepler K2*, *Transiting Exoplanet Survey Satellite (TESS)*, the *Planetary Transits and Oscillations of stars (PLATO)*, and *Characterizing Exoplanets Satellite (CHEOPS)* missions. Dramatic differences in the location of the desert for mid M dwarfs could be suggestive of flaring being an important contribution to atmospheric photoevaporation. Additional observational constraints on the frequency of flaring around mid M dwarfs will assist in this determination. Furthermore, a dedicated satellite for measuring extreme ultraviolet (EUV) fluxes will help to quantify the total contributions of high energy radiation to the photoevaporation process, instead of requiring extrapolation of X-ray behavior to the EUV. Finally, additional observations of the atmospheres of individual potentially photoevaporated planets can provide high precision constraints on the boundary of the photoevaporation desert. Depending on the flaring activity of late M-type stars, the inner TRAPPIST-1 planets (particularly planets b and c) may receive sufficient high energy radiation to be fully or partially evaporated, motivating follow-up observations [Gillon

et al., 2017]. All of these follow-up studies will help in the assessment of the habitability of close-in planets around low mass stars—not only in the context of the stability of their atmospheres, but also in consideration of the extent that high energy radiation would cause genetic mutations on any putative life forms.

Concerning studies of Titan's surface composition using infrared spectroscopy, the work herein has focused primarily on the spectral domain and the atmospheric effects therein. Consideration of the spatial domain will be important to understand the extent to which spectroscopy could detect molecules of prebiotic interest. For example, whether relatively complex molecules such as amino acids and nucleobases can be found in high enough concentrations to occupy significant fractions of spectrometer pixels for remote observation is an important consideration. This will also require consideration of physical constraints on instrument parameters—e.g. maximum telescope sizes and detector sensitivities that could be deployed on a mission that must operate aerially. Furthermore, continued refinement of radiative transfer models such that they could be used in interpreting future data take in Titan's near-surface environment will be paramount—localized variations in methane humidity, interpreting observations with high emission angles, possible geographical variations in haze composition must all be able to modeled effectively for robust detections of surface compounds. Of course, our actual understanding of Titan's surface composition at the level of specific molecules will continue to be limited until the actual deployment of a mission in Titan's near-surface environment.

In the broader context, studies of atmospheric radiative properties will continue to be critical in the quest to understand all of the combined effects that makes a planetary body habitable. In the context of the solar system, a more detailed understanding of the sensitivity of atmospheric H and O escape at Venus to solar conditions and geographic location will aid in the extrapolation of atmospheric escape rates to earlier in Venus's history. This would help in estimating early Venus's water content and prospensity for holding standing liquid water [Tian et al., 2013]. On Mars, recent observations are suggestive of present-day

liquid water in the form of brines [Ojha et al., 2015]. Confirmation that the recurring slope lineae (RSL) are indeed liquid water must consider whether nighttime relative humidities could be high enough to drive the RSL, as well as more detailed observations of the possible link between low lying atmospheric water ice and the RSL [Ojha et al., 2017]. For exoplanets, in addition to the importance of increasing the sample size of known planets in the habitable zone around late type stars, direct spectroscopic observations of the atmospheres of nearby rocky planets [Kreidberg and Loeb, 2016] will be made possible by the *James Webb Space Telescope*. This will allow for detailed case studies of how particular atmospheric compositions lend themselves to the possibility of standing liquid water and complex surficial organic chemistry.

BIBLIOGRAPHY

M. Ádámkovics and J. L. Mitchell. Search for methane isotope fractionation due to Rayleigh distillation on Titan. *Icarus*, 275:232–238, 2016. ISSN 10902643. doi: 10.1016/j.icarus.2016.04.006.

V. S. Airapetian, A. Glocer, G. V. Khazanov, R. O. P. Loyd, K. France, J. Sojka, W. C. Danchi, and M. W. Liemohn. How Hospitable Are Space Weather Affected Habitable Zones? The Role of Ion Escape. *The Astrophysical Journal*, 2017. ISSN 2041-8213. doi: 10.3847/2041-8213/836/1/L3.

T. Anderson and D. Darling. A Test of Goodness o Fit. *Journal of the American Statistical Association*, 49(268):765–769, 1954.

K. Baines, S. Atreya, M. Bullock, D. Grinspoon, P. Mahaffy, C. Russel, G. Schubert, and K. Zahnle. A Social relations model for the colonial behaviour of the Zebra finch. In *Comparative Climatology of Terrestrial Planets*, volume 1, pages 137–160. 2013. ISBN 9780816530595. doi: 10.2458/azu. URL http://arxiv.org/abs/1306.2418.

I. Baraffe, Y. Alibert, G. Chabrier, and W. Benz. Birth and fate of hot-Neptune planets. *Astronomy and Astrophysics*, 450:1221, 2006. ISSN 1432-0746. doi: 10.1051/0004-6361:20054040. URL http://adsabs.harvard.edu/cgi-bin/nph-data{_}query?bibcode=2006A{%}2526A...450.1221B{&}link{_}type=ABSTRACT{%}5Cnpapers://0be24a46-325a-4116-a3c6-fd8a3b614472/Paper/p16.

I. Baraffe, D. Homeier, F. Allard, and G. Chabrier. Astrophysics New evolutionary models for pre-main sequence and main sequence low-mass stars down to the hydrogen-burning limit. *Astronomy & Astrophysics*, A42:4–9, 2015.

J. W. Barnes, R. H. Brown, E. P. Turtle, A. S. McEwen, R. D. Lorenz, M. Janssen, E. L. Schaller, M. E. Brown, B. J. Buratti, C. Sotin, C. Griffith, R. Clark, J. Perry, S. Fussner, J. Barbara, R. West, C. Elachi, A. H. Bouchez, H. G. Roe, K. H. Baines, G. Bellucci, J.-P. Bibring, F. Capaccioni, P. Cerroni, M. Combes, A. Coradini, D. P. Cruikshank, P. Drossart, V. Formisano, R. Jaumann, Y. Langevin, D. L. Matson, T. B. McCord, P. D. Nicholson, and B. Sicardy. A 5-micron-bright spot on Titan: evidence for surface diversity. *Science (New York, N.Y.)*, 310(5745):92–5, 2005. ISSN 1095-9203. doi: 10.1126/science.1117075. URL `http://www.ncbi.nlm.nih.gov/pubmed/16210535`.

J. W. Barnes, R. H. Brown, L. Soderblom, C. Sotin, S. Le Mouèlic, S. Rodriguez, R. Jaumann, R. A. Beyer, B. J. Buratti, K. Pitman, K. H. Baines, R. Clark, and P. Nicholson. Spectroscopy, morphometry, and photoclinometry of Titan's dunefields from Cassini/VIMS. *Icarus*, 195(1):400–414, 2008. ISSN 00191035. doi: 10.1016/j.icarus.2007.12.006.

J. W. Barnes, L. Lemke, R. Foch, C. P. McKay, R. A. Beyer, J. Radebaugh, D. H. Atkinson, R. D. Lorenz, S. Le Mou??lic, S. Rodriguez, J. Gundlach, F. Giannini, S. Bain, F. M. Flasar, T. Hurford, C. M. Anderson, J. Merrison, M. ??d??mkovics, S. A. Kattenhorn, J. Mitchell, D. M. Burr, A. Colaprete, E. Schaller, A. J. Friedson, K. S. Edgett, A. Coradini, A. Adriani, K. M. Sayanagi, M. J. Malaska, D. Morabito, and K. Reh. AVIATR-Aerial Vehicle for In-situ and Airborne Titan Reconnaissance. *Experimental Astronomy*, 33(1):55–127, 2012. ISSN 09226435. doi: 10.1007/s10686-011-9275-9.

A. Bressan, P. Marigo, L. Girardi, B. Salasnich, C. Dal Cero, S. Rubele, and A. Nanni. Parsec: Stellar tracks and isochrones with the PAdova and TRieste Stellar Evolution Code. *Monthly Notices of the Royal Astronomical Society*, 427(1):127–145, 2012. ISSN 00358711. doi: 10.1111/j.1365-2966.2012.21948.x.

A. J. Brown, S. Byrne, L. L. Tornabene, and T. Roush. Louth crater: Evolution of a layered

water ice mound. *Icarus*, 196(2):433–445, 2008. ISSN 00191035. doi: 10.1016/j.icarus.2007.11.023.

A. S. Burton, J. C. Stern, J. E. Elsila, D. P. Glavin, and J. P. Dworkin. Understanding prebiotic chemistry through the analysis of extraterrestrial amino acids and nucleobases in meteorites. *Chemical Society Reviews*, 41(16):5459–5472, 2012. ISSN 03060012. doi: 10.1039/c2cs35109a.

A. Campargue, L. Wang, D. Mondelain, S. Kassi, B. Bézard, E. Lellouch, A. Coustenis, C. de Bergh, M. Hirtzig, and P. Drossart. An empirical line list for methane in the 1.26-1.71μm region for planetary investigations (T=80-300K). Application to Titan. *Icarus*, 2012. ISSN 00191035. doi: 10.1016/j.icarus.2012.02.015.

H. Chen and L. A. Rogers. Evolutionary Analysis of Gaseous Sub-Neptune-Mass Planets with MESA. *The Astrophysical Journal*, 831(2):1–18, 2016. ISSN 1538-4357. doi: 10.3847/0004-637X/831/2/180. URL `http://arxiv.org/abs/1603.06596{%}0Ahttp://dx.doi.org/10.3847/0004-637X/831/2/180`.

Y. Chen, L. Girardi, A. Bressan, P. Marigo, M. Barbieri, and X. Kong. Improving PARSEC models for very low mass stars. *Monthly Notices of the Royal Astronomical Society*, 444 (3):2525–2543, 2014. ISSN 13652966. doi: 10.1093/mnras/stu1605.

R. N. Clark, J. M. Curchin, J. W. Barnes, R. Jaumann, L. Soderblom, D. P. Cruikshank, R. H. Brown, S. Rodriguez, J. Lunine, K. Stephan, T. M. Hoefen, S. Le Mouélic, C. Sotin, K. H. Baines, B. J. Buratti, and P. D. Nicholson. Detection and mapping of hydrocarbon deposits on Titan. *Journal of Geophysical Research E: Planets*, 115(10), 2010. ISSN 01480227. doi: 10.1029/2009JE003369.

C. De Bergh, R. Courtin, B. Bézard, A. Coustenis, E. Lellouch, M. Hirtzig, P. Rannou, P. Drossart, A. Campargue, S. Kassi, L. Wang, V. Boudon, A. Nikitin, and V. Tyuterev. Applications of a new set of methane line parameters to the modeling of Titan's spectrum

in the 1.58 μm window. In *Planetary and Space Science*, 2012. doi: 10.1016/j.pss.2011.05.003.

I. de Pater and J. J. Lissauer. *Planetary Sciences*. Cambridge University Press, Cambridge, 2015. ISBN 9781316165270. doi: 10.1017/CBO9781316165270. URL http://ebooks.cambridge.org/ref/id/CBO9781316165270.

M. L. Delitsky and C. P. McKay. The photochemical products of benzene in Titan's upper atmosphere. *Icarus*, 2010. ISSN 00191035. doi: 10.1016/j.icarus.2009.11.002.

F. M. Flasar, R. K. Achterberg, B. J. Conrath, P. J. Gierasch, V. G. Kunde, C. A. Nixon, G. L. Bjoraker, D. E. Jennings, P. N. Romani, A. A. Simon-Miller, B. Bézard, A. Coustenis, P. G. Irwin, N. A. Teanby, J. Brasunas, J. C. Pearl, M. E. Segura, R. C. Carlson, A. Mamoutkine, P. J. Schinder, A. Barucci, R. Courtin, T. Fouchet, D. Gautier, E. Lellouch, A. Marten, R. Prangé, S. Vinatier, D. F. Strobel, S. B. Calcutt, P. L. Read, F. W. Taylor, N. Bowles, R. E. Samuelson, G. S. Orton, L. J. Spilker, T. C. Owen, J. R. Spencer, M. R. Showalter, C. Ferrari, M. M. Abbas, F. Raulin, S. Edgington, P. Ade, and E. H. Wishnow. Titan's atmospheric temperatures, winds, and composition. *Science*, 2005. ISSN 00368075. doi: 10.1126/science.1111150.

D. Foreman-Mackey, D. W. Hogg, D. Lang, and J. Goodman. emcee: The MCMC Hammer. pages 306–312, 2012. ISSN 00046280. doi: 10.1086/670067. URL http://arxiv.org/abs/1202.3665{%}0Ahttp://dx.doi.org/10.1086/670067.

D. Foreman-Mackey, D. W. Hogg, and T. D. Morton. Exoplanet population inference and the abundance of earth analogs from noisy, incomplete catalogs. *Astrophysical Journal*, 795(1), 2014. ISSN 15384357. doi: 10.1088/0004-637X/795/1/64.

F. Fressin, G. Torres, D. Charbonneau, S. T. Bryson, J. Christiansen, C. D. Dressing, J. M. Jenkins, L. M. Walkowicz, and N. M. Batalha. THE FALSE POSITIVE RATE

OF KEPLER AND THE OCCURRENCE OF PLANETS. *The Astrophysical Journal*, 766(2):81, 2013. ISSN 0004-637X. doi: 10.1088/0004-637X/766/2/81. URL http://stacks.iop.org/0004-637X/766/i=2/a=81?key=crossref.61220c7d574853ef276f8ffca21a3682.

B. J. Fulton, E. A. Petigura, A. W. Howard, H. Isaacson, G. W. Marcy, P. A. Cargile, L. Hebb, L. M. Weiss, J. A. Johnson, T. D. Morton, E. Sinukoff, I. J. M. Crossfield, and L. A. Hirsch. The California-Kepler Survey. III. A Gap in the Radius Distribution of Small Planets. *The Astronomical Journal*, 109, 2017. ISSN 1538-3881. doi: 10.3847/1538-3881/aa80eb. URL http://arxiv.org/abs/1703.10375{%}0Ahttp://dx.doi.org/10.3847/1538-3881/aa80eb.

M. Gillon, A. H. Triaud, B. O. Demory, E. Jehin, E. Agol, K. M. Deck, S. M. Lederer, J. De Wit, A. Burdanov, J. G. Ingalls, E. Bolmont, J. Leconte, S. N. Raymond, F. Selsis, M. Turbet, K. Barkaoui, A. Burgasser, M. R. Burleigh, S. J. Carey, A. Chaushev, C. M. Copperwheat, L. Delrez, C. S. Fernandes, D. L. Holdsworth, E. J. Kotze, V. Van Grootel, Y. Almleaky, Z. Benkhaldoun, P. Magain, and D. Queloz. Seven temperate terrestrial planets around the nearby ultracool dwarf star TRAPPIST-1. *Nature*, 2017. ISSN 14764687. doi: 10.1038/nature21360.

S. Ginzburg, H. E. Schlichting, and R. Sari. Core-powered mass loss sculpts the radius distribution of small exoplanets. *Monthly Notices of the Royal Astronomical Society*, 765(March):759–765, 2017. ISSN 0035-8711. doi: 10.1093/mnras/sty290/4839004. URL http://arxiv.org/abs/1708.01621.

I. E. Gordon, L. S. Rothman, C. Hill, R. V. Kochanov, Y. Tan, P. F. Bernath, M. Birk, V. Boudon, A. Campargue, K. V. Chance, B. J. Drouin, J. M. Flaud, R. R. Gamache, J. T. Hodges, D. Jacquemart, V. I. Perevalov, A. Perrin, K. P. Shine, M. A. Smith, J. Tennyson, G. C. Toon, H. Tran, V. G. Tyuterev, A. Barbe, A. G. Császár, V. M. Devi, T. Furtenbacher, J. J. Harrison, J. M. Hartmann, A. Jolly, T. J. Johnson, T. Karman,

I. Kleiner, A. A. Kyuberis, J. Loos, O. M. Lyulin, S. T. Massie, S. N. Mikhailenko, N. Moazzen-Ahmadi, H. S. Müller, O. V. Naumenko, A. V. Nikitin, O. L. Polyansky, M. Rey, M. Rotger, S. W. Sharpe, K. Sung, E. Starikova, S. A. Tashkun, J. V. Auwera, G. Wagner, J. Wilzewski, P. Wcisło, S. Yu, and E. J. Zak. The HITRAN2016 molecular spectroscopic database. *Journal of Quantitative Spectroscopy and Radiative Transfer*, 2017. ISSN 00224073. doi: 10.1016/j.jqsrt.2017.06.038.

C. A. Griffith, L. Doose, M. G. Tomasko, P. F. Penteado, and C. See. Radiative transfer analyses of Titan's tropical atmosphere. *Icarus*, 218(2):975–988, 2012. ISSN 00191035. doi: 10.1016/j.icarus.2011.11.034. URL `http://dx.doi.org/10.1016/j.icarus.2011.11.034`.

A. Hayes, O. Aharonson, P. Callahan, C. Elachi, Y. Gim, R. Kirk, K. Lewis, R. Lopes, R. Lorenz, J. Lunine, K. Mitchell, G. Mitri, E. Stofan, and S. Wall. Hydrocarbon lakes on Titan: Distribution and interaction with a porous regolith. *Geophysical Research Letters*, 35(9):1–6, 2008. ISSN 00948276. doi: 10.1029/2008GL033409.

M. Hirtzig, B. Bézard, E. Lellouch, A. Coustenis, C. de Bergh, P. Drossart, A. Campargue, V. Boudon, V. Tyuterev, P. Rannou, T. Cours, S. Kassi, A. Nikitin, D. Mondelain, S. Rodriguez, and S. Le Mouélic. Titan's surface and atmosphere from Cassini/VIMS data with updated methane opacity. *Icarus*, 226(1):470–486, 2013. ISSN 00191035. doi: 10.1016/j.icarus.2013.05.033. URL `http://dx.doi.org/10.1016/j.icarus.2013.05.033`.

K. L. Hoffman and J. F. Rowe. Uniform Modeling of KOIs : MCMC Notes for Data Release 25. Technical Report April, NASA Ames Research Center, Moffett Field, CA, 2017.

A. W. Howard, G. W. Marcy, S. T. Bryson, J. M. Jenkins, J. F. Rowe, N. M. Batalha, W. J. Borucki, D. G. Koch, E. W. Dunham, T. N. Gautier, J. Van Cleve, W. D. Cochran,

D. W. Latham, J. J. Lissauer, G. Torres, T. M. Brown, R. L. Gilliland, L. A. Buchhave, D. A. Caldwell, J. Christensen-Dalsgaard, D. Ciardi, F. Fressin, M. R. Haas, S. B. Howell, H. Kjeldsen, S. Seager, L. Rogers, D. D. Sasselov, J. H. Steffen, G. S. Basri, D. Charbonneau, J. Christiansen, B. Clarke, A. Dupree, D. C. Fabrycky, D. A. Fischer, E. B. Ford, J. J. Fortney, J. Tarter, F. R. Girouard, M. J. Holman, J. A. Johnson, T. C. Klaus, P. Machalek, A. V. Moorhead, R. C. Morehead, D. Ragozzine, P. Tenenbaum, J. D. Twicken, S. N. Quinn, H. Isaacson, A. Shporer, P. W. Lucas, L. M. Walkowicz, W. F. Welsh, A. Boss, E. Devore, A. Gould, J. C. Smith, R. L. Morris, A. Prsa, T. D. Morton, M. Still, S. E. Thompson, F. Mullally, M. Endl, and P. J. MacQueen. Planet occurrence within 0.25 AU of solar-type stars form Kepler. *The Astrophysical Journal Supplement Series*, 201(2):15, 2012. ISSN 0067-0049. doi: 10.1088/0067-0049/201/2/15. URL `http://stacks.iop.org/0067-0049/201/i=2/a=15?key=crossref.bb652de4e99bfc1aec39c97d5f92480e`.

A. P. Jackson, T. A. Davis, and P. J. Wheatley. The coronal X-ray-age relation and its implications for the evaporation of exoplanets. *Monthly Notices of the Royal Astronomical Society*, 422(3):2024–2043, 2012. ISSN 00358711. doi: 10.1111/j.1365-2966.2012.20657.x.

B. Jackson, N. Miller, R. Barnes, S. N. Raymond, J. J. Fortney, and R. Greenberg. The roles of tidal evolution and evaporative mass loss in the origin of CoRoT-7 b. *Monthly Notices of the Royal Astronomical Society*, 407(2):910–922, 2010. ISSN 00358711. doi: 10.1111/j.1365-2966.2010.17012.x.

Y. A. Jeilani, C. Fearce, and M. T. Nguyen. Acetylene as an essential building block for prebiotic formation of pyrimidine bases on Titan. *Physical Chemistry Chemical Physics*, 2015. ISSN 14639076. doi: 10.1039/c5cp03247d.

S. Jin and C. Mordasini. Compositional imprints in density-distance-time: a rocky composition for close-in low-mass exoplanets from the location of the valley of evapora-

tion. *The Astrophysical Journal*, 853(2):163, 2017. ISSN 1538-4357. doi: 10.3847/1538-4357/aa9f1e. URL http://arxiv.org/abs/1706.00251.

J. A. Johnson, E. A. Petigura, B. J. Fulton, G. W. Marcy, W. Andrew, H. Isaacson, L. Hebb, P. A. Cargile, T. D. Morton, L. M. Weiss, J. N. Winn, L. A. Rogers, E. Sinukoff, and L. A. Hirsch. The california-kepler survey. ii. precise physical properties of 2025 kepler planets and their host stars 1. *arXiv*, pages 1–11, 2017.

S. S. Johnson, M. A. Mischna, T. L. Grove, and M. T. Zuber. Sulfur-induced greenhouse warming on early Mars. *Journal of Geophysical Research E: Planets*, 2008. ISSN 01480227. doi: 10.1029/2007JE002962.

J. F. Kasting, D. P. Whitmire, and R. T. Reynolds. Habitable Zones around Main Sequence Stars. *Icarus*, 1993. ISSN 10902643. doi: 10.1006/icar.1993.1010.

B. N. Khare, C. Sagan, H. Ogino, B. Nagy, C. Er, K. H. Schram, and E. T. Arakawa. Amino acids derived from Titan Tholins. *Icarus*, 68(1):176–184, 1986. ISSN 10902643. doi: 10.1016/0019-1035(86)90080-1.

L. Kreidberg and A. Loeb. Prospects for Characterizing the Atmosphere of Proxima Centauri b. *The Astrophysical Journal Letters*, 832(1):1–6, 2016. ISSN 2041-8213. doi: 10.3847/2041-8205/832/1/L12. URL http://arxiv.org/abs/1608.07345{%}0Ahttp://dx.doi.org/10.3847/2041-8205/832/1/L12.

G. P. Kuiper. Titan: A satellite with an atmosphere. *Astrophysical Journal*, (99), 1944.

A. Lecavelier Des Etangs. A diagram to determine the evaporation status of extrasolar planets. *Astronomy and Astrophysics*, 461:1185, 2007. ISSN 1432-0746. doi: 10.1051/0004-6361:20065014. URL http://adsabs.harvard.edu/cgi-bin/nph-data{_}query?bibcode=2007A{%}2526A...461.1185L{&}link{_}type=ABSTRACT{%}5Cnpapers://0be24a46-325a-4116-a3c6-fd8a3b614472/Paper/p4269.

K. Liou. *Introduction to Atmospheric Radiation (2nd Edition)*. Elsevier, 2002. URL http://app.knovel.com/web/toc.v/cid:kpIARE0015.

R. M. C. Lopes, R. L. Kirk, K. L. Mitchell, A. Legall, J. W. Barnes, A. Hayes, J. Kargel, L. Wye, J. Radebaugh, E. R. Stofan, M. A. Janssen, C. D. Neish, S. D. Wall, C. A. Wood, J. I. Lunine, and M. J. Malaska. Cryovolcanism on Titan: New results from Cassini RADAR and VIMS. *Journal of Geophysical Research E: Planets*, 118(3):416–435, 2013. ISSN 01480227. doi: 10.1002/jgre.20062.

E. D. Lopez. Born Dry in the Photo-Evaporation Desert: Kepler's Ultra-Short-Period Planets Formed Water-Poor. *Monthly Notices of the Royal Astronomical Society*, 253(March):245–253, 2016. ISSN 0035-8711. doi: 10.1093/mnras/stx1558. URL http://arxiv.org/abs/1610.01170{%}0Ahttp://dx.doi.org/10.1093/mnras/stx1558.

E. D. Lopez and J. J. Fortney. the Role of Core Mass in Controlling Evaporation: the Kepler Radius Distribution and the Kepler-36 Density Dichotomy. *The Astrophysical Journal*, 776(1):2, 2013. ISSN 0004-637X. doi: 10.1088/0004-637X/776/1/2. URL http://stacks.iop.org/0004-637X/776/i=1/a=2?key=crossref.f3eace3c36bf214df3c6e62a299080f0.

E. D. Lopez and J. J. Fortney. Understanding the Mass-Radius Relation for Sub-Neptunes: Radius As a Proxy for Composition. *The Astrophysical Journal*, 792(1):1, 2014. ISSN 1538-4357. doi: 10.1088/0004-637X/792/1/1. URL http://stacks.iop.org/0004-637X/792/i=1/a=1?key=crossref.de6c64a530eb6a60f7498f6c4dbcac24.

E. D. Lopez and K. Rice. Predictions for the Period Dependence of the Transition Between Rocky Super-Earths and Gaseous Sub-Neptunes and Implications for eta-Earth. 8 (November):1–8, 2016. URL http://arxiv.org/abs/1610.09390.

E. D. Lopez, J. J. Fortney, and N. Miller. How Thermal Evolution and Mass-Loss Sculpt Populations of Super-Earths and Sub-Neptunes: Application To the Kepler-11 System and Beyond. *The Astrophysical Journal*, 761(1):59, 2012. ISSN 0004-637X. doi: 10.1088/0004-637X/761/1/59. URL http://stacks.iop.org/0004-637X/761/i=1/a=59?key=crossref.d4c174a3db55c1a582360cec02f0a7a6.

R. D. Lorenz. A Review of Ballon Concepts for Titan. *Journal of the British Interplanetary Society*, 61(1):2–13, 2008.

M. S. Lundkvist, H. Kjeldsen, S. Albrecht, G. R. Davies, S. Basu, D. Huber, A. B. Justesen, C. Karoff, V. Silva Aguirre, V. Van Eylen, C. Vang, T. Arentoft, T. Barclay, T. R. Bedding, T. L. Campante, W. J. Chaplin, J. Christensen-Dalsgaard, Y. P. Elsworth, R. L. Gilliland, R. Handberg, S. Hekker, S. D. Kawaler, M. N. Lund, T. S. Metcalfe, A. Miglio, J. F. Rowe, D. Stello, B. Tingley, and T. R. White. Hot super-Earths stripped by their host stars. *Nature communications*, 7:11201, 2016. ISSN 2041-1723. doi: 10.1038/ncomms11201. URL http://arxiv.org/abs/1604.05220.

S. M. MacKenzie and J. W. Barnes. COMPOSITIONAL SIMILARITIES AND DISTINCTIONS BETWEEN TITAN'S EVAPORITIC TERRAINS. *The Astrophysical Journal*, 821(1):17, apr 2016. ISSN 1538-4357. doi: 10.3847/0004-637X/821/1/17. URL http://stacks.iop.org/0004-637X/821/i=1/a=17?key=crossref.bbbf9be7482619ae5669307abb012ab0.

M. Mastrogiuseppe and V. Poggiali. the bathymetry of a Titna sea. *Geophysical ...*, pages 1432–1437, 2014. doi: 10.1002/2013GL058618.Received. URL http://onlinelibrary.wiley.com/doi/10.1002/2013GL058618/full.

M. Mastrogiuseppe, A. G. Hayes, V. Poggiali, J. I. Lunine, R. D. Lorenz, R. Seu, A. Le Gall, C. Notarnicola, K. L. Mitchell, M. Malaska, and S. P. Birch. Bathymetry and composition of Titan's Ontario Lacus derived from Monte Carlo-based waveform in-

version of Cassini RADAR altimetry data. *Icarus*, 2018. ISSN 10902643. doi: 10.1016/j.icarus.2017.09.009.

S. Mathur, D. Huber, M. R. Haas, and N. M. Batalha. Keller Stellar Properties Catalog Update for Q1-17 DR25 Transit Search. Technical Report January, NASA Ames Research Center, Moffett Field, CA, 2016.

T. Mazeh, T. Holczer, and S. Faigler. Dearth of short-period Neptunian exoplanets - a desert in period-mass and period-radius planes. *Astronomy & Astrophysics*, A75:1–7, 2016. ISSN 0004-6361. doi: 10.1051/0004-6361/201528065. URL http://arxiv.org/abs/1602.07843{%}0Ahttp://dx.doi.org/10.1051/0004-6361/201528065.

T. B. McCord, P. Hayne, J. P. Combe, G. B. Hansen, J. W. Barnes, S. Rodriguez, S. Le Mouélic, E. K. H. Baines, B. J. Buratti, C. Sotin, P. Nicholson, R. Jaumann, R. Nelson, and the Cassini VIMS Team. *Titan's surface: Search for spectral diversity and composition using the Cassini VIMS investigation*, volume 194. 2008. ISBN 1487118864. doi: 10.1016/j.icarus.2007.08.039.

A. R. W. McKellar. Low-temperature infrared absorption of gaseous N2 and N2 + H2 in the 2.0-2.5 ??m region: Application to the atmospheres of Titan and Triton. *Icarus*, 80 (2):361–369, 1989. ISSN 10902643. doi: 10.1016/0019-1035(89)90146-2.

R. J. Michaelides, A. G. Hayes, M. Mastrogiuseppe, H. A. Zebker, T. G. Farr, M. J. Malaska, V. Poggiali, and J. P. Mullen. Constraining the physical properties of Titan's empty lake basins using nadir and off-nadir Cassini RADAR backscatter. *Icarus*, 270:57–66, 2016. ISSN 10902643. doi: 10.1016/j.icarus.2015.09.043. URL http://dx.doi.org/10.1016/j.icarus.2015.09.043.

S. L. Miller and H. C. Urey. Organic compound synthesis on the primitive earth. *Science*, 1959. ISSN 00368075. doi: 10.1126/science.130.3370.245.

K. L. Mitchell, M. B. Barmatz, C. S. Jamieson, R. D. Lorenz, and J. I. Lunine. Laboratory measurements of cryogenic liquid alkane microwave absorptivity and implications for the composition of Ligeia Mare, Titan. *Geophysical Research Letters*, 42(5):1340–1345, 2015. ISSN 19448007. doi: 10.1002/2014GL059475.

T. D. Morton, S. T. Bryson, J. L. Coughlin, J. F. Rowe, G. Ravichandran, E. A. Petigura, M. R. Haas, and N. M. Batalha. False Positive Probabilities for All Kepler Objects of Interest: 1284 Newly Validated Planets and 428 Likely False Positives. *The Astrophysical Journal*, 822(2):86, 2016. ISSN 1538-4357. doi: 10.3847/0004-637X/822/2/86. URL http://arxiv.org/abs/1605.02825{%}5Cnhttp://dx.doi.org/10.3847/0004-637X/822/2/86{%}5Cnhttp://stacks.iop.org/0004-637X/822/i=2/a=86?key=crossref.e345841835057fd3f4a9801db35b5dc7.

R. A. Murray-Clay, E. I. Chiang, and N. Murray. Atmospheric Escape From Hot Jupiters. *The Astrophysical Journal*, 693(1):23–42, 2009. ISSN 0004-637X. doi: 10.1088/0004-637X/693/1/23. URL http://stacks.iop.org/0004-637X/693/i=1/a=23?key=crossref.d1003bf7304271525058608b157faac7.

C. D. Neish, a. Somogyi, H. Imanaka, J. I. Lunine, and M. a. Smith. Rate measurements of the hydrolysis of complex organic macromolecules in cold aqueous solutions: implications for prebiotic chemistry on the early Earth and Titan. *Astrobiology*, 8(2):273–287, 2008. ISSN 1531-1074. doi: 10.1089/ast.2007.0193.

C. D. Neish, Á. Somogyi, J. I. Lunine, and M. A. Smith. Low temperature hydrolysis of laboratory tholins in ammonia-water solutions: Implications for prebiotic chemistry on Titan. *Icarus*, 201(1):412–421, 2009. ISSN 00191035. doi: 10.1016/j.icarus.2009.01.003. URL http://dx.doi.org/10.1016/j.icarus.2009.01.003.

M. J. Nguyen, F. Raulin, P. Coll, S. Derenne, C. Szopa, G. Cernogora, G. Israël, and

J. M. Bernard. Carbon isotopic enrichment in Titan's tholins? Implications for Titan's aerosols. *Planetary and Space Science*, 55(13):2010–2014, 2007. ISSN 00320633. doi: 10.1016/j.pss.2007.04.010.

H. B. Niemann, S. K. Atreya, J. E. Demick, D. Gautier, J. A. Haberman, D. N. Harpold, W. T. Kasprzak, J. I. Lunine, T. C. Owen, and F. Raulin. Composition of Titan's lower atmosphere and simple surface volatiles as measured by the Cassini-Huygens probe gas chromatograph mass spectrometer experiment. *Journal of Geophysical Research E: Planets*, 115(12):1–22, 2010. ISSN 01480227. doi: 10.1029/2010JE003659.

C. A. Nixon, B. Temelso, S. Vinatier, N. A. Teanby, B. Bézard, R. K. Achterberg, K. E. Mandt, C. D. Sherrill, P. G. Irwin, D. E. Jennings, P. N. Romani, A. Coustenis, and F. M. Flasar. Isotopic ratios in titan's methane: Measurements and modeling. *Astrophysical Journal*, 2012. ISSN 15384357. doi: 10.1088/0004-637X/749/2/159.

L. Ojha, M. B. Wilhelm, S. L. Murchie, A. S. Mcewen, J. J. Wray, J. Hanley, M. Massé, and M. Chojnacki. Spectral evidence for hydrated salts in recurring slope lineae on Mars. *Nature Geoscience*, (September):1–5, 2015. ISSN 1752-0894. doi: 10.1038/NGEO2546.

L. Ojha, M. Chojnacki, G. D. McDonald, A. Shumway, M. J. Wolff, M. D. Smith, A. S. McEwen, K. Ferrier, C. Huber, J. J. Wray, and A. Toigo. Seasonal Slumps in Juventae Chasma, Mars. *Journal of Geophysical Research: Planets*, 122(10):2193–2214, 2017. ISSN 21699100. doi: 10.1002/2017JE005375.

J. E. Owen and A. P. Jackson. Planetary evaporation by UV & X-ray radiation: basic hydrodynamics. *Monthly Notices of the Royal Astronomical Society*, 425:2931, 2012. ISSN 1365-2966. doi: 10.1111/j.1365-2966.2012.21481.x. URL `http://adsabs.harvard.edu/cgi-bin/nph-data{_}query?bibcode=`

2012MNRAS.425.2931O{&}link{_}type=ABSTRACT{%}5Cnpapers://0be24a46-325a-4116-a3c6-fd8a3b614472/Paper/p11876.

J. E. Owen and S. Mohanty. Habitability of terrestrial-mass planets in the HZ of M Dwarfs - I. H/He-dominated atmospheres. *Monthly Notices of the Royal Astronomical Society*, 2016. ISSN 13652966. doi: 10.1093/mnras/stw959.

J. E. Owen and Y. Wu. Kepler Planets: A Tale of Evaporation. *The Astrophysical Journal*, 775(2):105, 2013. ISSN 0004-637X. doi: 10.1088/0004-637X/775/2/105. URL http://stacks.iop.org/0004-637X/775/i=2/a=105?key=crossref.e7e3b8a4cbf77823b77f072c0df4a905.

J. E. Owen and Y. Wu. The evaporation valley in the Kepler planets. *The Astrophysical Journal*, 29, 2017. ISSN 1538-4357. doi: 10.3847/1538-4357/aa890a. URL http://arxiv.org/abs/1705.10810{%}0Ahttp://dx.doi.org/10.3847/1538-4357/aa890a.

M. J. Pecaut and E. E. Mamajek. Intrinsic Colors, Temperatures, and Bolometric Corrections of Pre-Main-Sequence Stars. *The Astrophysical Journal Supplement Series*, 208(1):9, 2013. ISSN 0067-0049. doi: 10.1088/0067-0049/208/1/9. URL http://stacks.iop.org/0067-0049/208/i=1/a=9?key=crossref.40637725e05e58390e6b2c1741c9f4ac.

E. A. Petigura, A. W. Howard, and G. W. Marcy. Prevalence of Earth-size planets orbiting Sun-like stars. *Proceedings of the National Academy of Sciences*, 110(48):19273–19278, 2013a. ISSN 0027-8424. doi: 10.1073/pnas.1319465110. URL http://www.pnas.org/cgi/doi/10.1073/pnas.1319465110.

E. A. Petigura, G. W. Marcy, and A. W. Howard. a Plateau in the Planet Population Below Twice the Size of Earth. *The Astrophysical Journal*, 770(1):69, 2013b. ISSN 0004-637X. doi: 10.1088/0004-637X/770/1/

69. URL http://stacks.iop.org/0004-637X/770/i=1/a=69?key=crossref.64acd52dcf1eaabf97d8ba9093fcf7b1.

E. A. Petigura, A. W. Howard, G. W. Marcy, J. A. Johnson, H. Isaacson, P. A. Cargile, L. Hebb, B. J. Fulton, L. M. Weiss, T. D. Morton, J. N. Winn, L. A. Rogers, E. Sinukoff, L. A. Hirsch, and I. J. M. Crossfield. The California-Kepler Survey. I. High Resolution Spectroscopy of 1305 Stars Hosting Kepler Transiting Planets. *The Astronomical Journal*, 107, 2017. ISSN 1538-3881. doi: 10.3847/1538-3881/aa80de. URL http://arxiv.org/abs/1703.10400{%}0Ahttp://dx.doi.org/10.3847/1538-3881/aa80de.

R. M. Ramirez, R. Kopparapu, M. E. Zugger, T. D. Robinson, R. Freedman, and J. F. Kasting. Warming early Mars with CO2 and H2. *Nature Geoscience*, 2013. ISSN 1752-0894. doi: 10.1038/ngeo2000.

F. Raulin. Astrobiology and habitability of Titan. *Space Science Reviews*, 2008. ISSN 00386308. doi: 10.1007/s11214-006-9133-7.

F. Raulin, C. Mckay, J. Lunine, and T. Owen. Titan's Astrobiology. In *Titan from Cassini-Huygens*, pages 215–233. Springer Science, 2009.

L. A. Rogers. MOST 1.6 EARTH-RADIUS PLANETS ARE NOT ROCKY. *The Astrophysical Journal*, 801(1):41, 2015. ISSN 1538-4357. doi: 10.1088/0004-637X/801/1/41. URL http://stacks.iop.org/0004-637X/801/i=1/a=41?key=crossref.2d8964914e4a589b6deed320855bd458.

R. Sanchis-Ojeda, S. Rappaport, J. N. Winn, M. C. Kotson, A. Levine, and I. E. Mellah. a Study of the Shortest-Period Planets Found With Kepler. *The Astrophysical Journal*, 787(18pp), 2014. ISSN 0004-637X. doi: 10.1088/0004-637X/787/1/47.

J. Sanz-Forcada, G. Micela, I. Ribas, a. M. T. Pollock, C. Eiroa, A. Velasco, E. Solano, and D. García-Álvarez. Estimation of the XUV radiation onto close planets and

their evaporation. *Astronomy & Astrophysics*, 532:A6, 2011. ISSN 0004-6361. doi: 10.1051/0004-6361/201116594. URL http://arxiv.org/abs/1105.0550{%}5Cnhttp://www.aanda.org/10.1051/0004-6361/201116594.

V. See, M. Jardine, A. A. Vidotto, P. Petit, S. C. Marsden, S. V. Jeffers, and J. D. do Nascimento. The effects of stellar winds on the magnetospheres and potential habitability of exoplanets. *Astronomy & Astrophysics*, 2014. ISSN 0004-6361. doi: 10.1051/0004-6361/201424323.

E. L. Shkolnik and T. S. Barman. Hazmat. I. the Evolution of Far-Uv and Near-Uv Emission From Early M Stars. *The Astronomical Journal*, 148(4):64, 2014. ISSN 1538-3881. doi: 10.1088/0004-6256/148/4/64. URL http://stacks.iop.org/1538-3881/148/i=4/a=64?key=crossref.16abcf045a34c756ee0cb527f0685be3.

L. A. Soderblom, R. L. Kirk, J. I. Lunine, J. A. Anderson, K. H. Baines, J. W. Barnes, J. M. Barrett, R. H. Brown, B. J. Buratti, R. N. Clark, D. P. Cruikshank, C. Elachi, M. A. Janssen, R. Jaumann, E. Karkoschka, S. L. Mouélic, R. M. Lopes, R. D. Lorenz, T. B. McCord, P. D. Nicholson, J. Radebaugh, B. Rizk, C. Sotin, E. R. Stofan, T. L. Sucharski, M. G. Tomasko, and S. D. Wall. Correlations between Cassini VIMS spectra and RADAR SAR images: Implications for Titan's surface composition and the character of the Huygens Probe Landing Site. *Planetary and Space Science*, 55(13):2025–2036, 2007. ISSN 00320633. doi: 10.1016/j.pss.2007.04.014.

L. A. Soderblom, J. W. Barnes, R. H. Brown, R. N. Clark, M. A. Janssen, T. B. McCord, H. B. Niemann, and M. G. Tomasko. Composition of titan's surface. *Titan from Cassini-Huygens*, pages 141–175, 2010.

A. Solomonidou, M. Hirtzig, A. Coustenis, E. Bratsolis, S. Le Mouélic, S. Rodriguez, K. Stephan, P. Drossart, C. Sotin, R. Jaumann, R. H. Brown, K. Kyriakopoulos, R. M. Lopes, G. Bampasidis, K. Stamatelopoulou-Seymour, and X. Moussas. Surface albedo

spectral properties of geologically interesting areas on Titan. *Journal of Geophysical Research E: Planets*, 2014. ISSN 21699100. doi: 10.1002/2014JE004634.

C. Sotin, K. Altwegg, R. H. Brown, K. Hand, J. I. Lunine, J. Soderblom, J. Spencer, and P. Tortora. Jet: Journey To Enceladus and Titan. *42nd Lunar and Planetary Science Conference*, pages 2–3, 2011. URL https://www.lpi.usra.edu/meetings/lpsc2011/pdf/1326.pdf.

C. Sotin, A. Hayes, M. Malaska, M. Mastrogiuseppe, E. Mazarico, J. Soderblom, P. Tortora, M. Trainer, and E. Turtle. OCEANUS: A New Frontiers mission concept to study Titan's potential habitability. *European Planetary Science Congress 2017*, 11:3–4, 2017.

J. Stevenson, J. Lunine, and P. Clancy. Membrane alternatives in worlds without oxygen: Creation of an azotosome. *Science Advances*, 1(February):e1400067–e1400067, 2015. ISSN 2375-2548. doi: 10.1126/sciadv.1400067. URL http://advances.sciencemag.org/cgi/doi/10.1126/sciadv.1400067.

E. Stofan, R. Lorenz, J. Lunine, E. B. Bierhaus, B. Clark, P. R. Mahaffy, and M. Ravine. TiME-the titan mare explorer. In *IEEE Aerospace Conference Proceedings*, 2013. ISBN 9781467318112. doi: 10.1109/AERO.2013.6497165.

S. E. Thompson, J. L. Coughlin, K. Hoffman, F. Mullally, J. L. Christiansen, C. J. Burke, S. Bryson, N. Batalha, M. R. Haas, J. Catanzarite, J. F. Rowe, G. Barentsen, D. A. Caldwell, B. D. Clarke, J. M. Jenkins, J. Li, D. W. Latham, J. J. Lissauer, S. Mathur, R. L. Morris, S. E. Seader, J. C. Smith, T. C. Klaus, J. D. Twicken, B. Wohler, R. Akeson, D. R. Ciardi, W. D. Cochran, T. Barclay, J. R. Campbell, W. J. Chaplin, D. Charbonneau, C. E. Henze, S. B. Howell, D. Huber, A. Prsa, S. V. Ramirez, T. D. Morton, J. Christensen-Dalsgaard, J. L. Dotson, L. Doyle, E. W. Dunham, A. K. Dupree, E. B. Ford, J. C. Geary, F. R. Girouard, H. Isaacson, H. Kjeldsen, J. H. Steffen, E. V. Quintana, D. Ragozzine, A. Shporer, V. S. Aguirre, M. Still, P. Tenenbaum, W. F. Welsh, A. Wolfgang, K. A.

Zamudio, D. G. Koch, and W. J. Borucki. Planetary Candidates Observed by Kepler. VIII. A Fully Automated Catalog With Measured Completeness and Reliability Based on Data Release 25. *arXiv*, 2017. URL http://arxiv.org/abs/1710.06758.

F. Tian, E. Chassefiere, F. Leblanc, and D. A. Brain. Atmosphere Escape and climatic evolution of terrestrial planets. In *Comparative Climatology of Terrestrial Planets*, volume 1, pages 567–581. 2013. ISBN 9780816530595. doi: 10.2458/azu. URL http://arxiv.org/abs/1306.2418.

M. G. Tomasko, B. Archinal, T. Becker, B. Bézard, M. Bushroe, M. Combes, D. Cook, a. Coustenis, C. de Bergh, L. E. Dafoe, L. Doose, S. Douté, a. Eibl, S. Engel, F. Gliem, B. Grieger, K. Holso, E. Howington-Kraus, E. Karkoschka, H. U. Keller, R. Kirk, R. Kramm, M. Küppers, P. Lanagan, E. Lellouch, M. Lemmon, J. Lunine, E. McFarlane, J. Moores, G. M. Prout, B. Rizk, M. Rosiek, P. Rueffer, S. E. Schröder, B. Schmitt, C. See, P. Smith, L. Soderblom, N. Thomas, and R. West. Rain, winds and haze during the Huygens probe's descent to Titan's surface. *Nature*, 438(December):765–778, 2005. ISSN 0028-0836. doi: 10.1038/nature04126.

M. G. Tomasko, L. Doose, S. Engel, L. E. Dafoe, R. West, M. Lemmon, E. Karkoschka, and C. See. A model of Titan's aerosols based on measurements made inside the atmosphere. *Planetary and Space Science*, 56(5):669–707, 2008. ISSN 00320633. doi: 10.1016/j.pss.2007.11.019.

E. P. Turtle, J. W. Barnes, M. G. Trainer, R. D. Lorenz, K. E. Hibbard, D. Adams, and P. Bedini. Dragonfly: in Situ Exploration of Titan'S Organic Chemistry and Habitability. In *European Planetary Science Congress*, volume 11, pages 349–4, 2017. doi: 10.1109/AERO.2013.6497165. URL http://www.lpi.usra.edu/meetings/lpsc2017/pdf/1958.pdf.

V. Vuitton, R. V. Yelle, and M. J. McEwan. Ion chemistry and N-containing molecules

in Titan's upper atmosphere. *Icarus*, 191(2):722–742, 2007. ISSN 00191035. doi: 10.1016/j.icarus.2007.06.023.

L. M. Weiss and G. W. Marcy. The mass-radius relation for 65 exoplanets smaller than 4 earth radii. *Astrophysical Journal Letters*, 783(1):1–7, 2014. ISSN 20418205. doi: 10.1088/2041-8205/783/1/L6.

A. Wolfgang and E. Lopez. How rocky are they? The composition distribution of Kepler's sub-Neptune planet candidates within 0.15 AU. *The Astrophysical Journal*, 806(2):183, 2015. ISSN 1538-4357. doi: 10.1088/0004-637X/806/2/183. URL http://stacks.iop.org/0004-637X/806/i=2/a=183?key=crossref.5cf17c111664baf03c7862f15219dfb2.

A. Wolfgang, L. A. Rogers, and E. B. Ford. Probabilistic Mass-Radius Relationship for Sub-Neptune-Sized Planets. *The Astrophysical Journal*, 825 (1):19, 2016. ISSN 1538-4357. doi: 10.3847/0004-637X/825/1/19. URL http://stacks.iop.org/0004-637X/825/i=1/a=19?key=crossref.0bb32f43171750dd154938682bf8144f.

R. V. Yelle. Aeronomy of extra-solar giant planets at small orbital distances. *Icarus*, 170 (1):167–179, 2004. ISSN 00191035. doi: 10.1016/j.icarus.2004.02.008.

VITA

George D. McDonald was born in Tokyo, Japan in 1991 and raised along with his sister Alice by James McDonald, a stock portfolio manager, and Yumi McDonald, a writer and journalist. He was raised primarily in Westport, Connecticut but with many formative years in Tokyo, Japan. George graduated high school at the American School in Japan. He then attended Cornell University where he studied physics and first began research, studying dunes on Titan, and graduated in 2014. George moved to Atlanta in 2014 to work on a PhD in Planetary Science at the Georgia Institute of Technology, completed in 2018. George looks forward to using his data analysis skills to improve public and alternative transportation as a Senior Performance Analyst at the Georgia Regional Transportation Authority, where he hopes his work will help mitigate climate change and improve public health. George has a passion for water sports, space, politics, scale model and miniature painting, and good urbanism. He lives in Atlanta, Georgia with Josh Méndez.